1. COVER PAGE DATA ELEMENTS

Federal Agency and Organization Element to Which Report is Submitted	U.S. Department of Energy National Energy Technology Laboratory
Federal Grant Number	DE-FE0031862
Project Title	Process Intensification by One-Step, Plasma-Assisted Catalytic Synthesis of Liquid Chemicals from Light Hydrocarbons
PD/PI Name, Title and Contact Information (e-mail address and phone number)	**Technical Contact (Principal Investigator):** Jason C. Hicks, Professor jhicks3@nd.edu, (574) 631-3661 **Business Contact:** Ann Strasser, Assistant Controller researc2@nd.edu, (574) 631-5437
Name of Submitting Official, Title, and Contact Information (e-mail address and phone number)	Jason C. Hicks, Tony and Sarah Earley Collegiate Professor of Energy and the Environment, jhicks3@nd.edu, (574) 631-3661
Submission Date	March 6, 2024
UEI	FPU6XGFXMBE9
DUNS Number	824910376
Recipient Organization (Name and Address)	University of Notre Dame 940 Grace Hall Notre Dame, St. Joseph County IN 46556-5708
Project/Grant Period (Start Date, End Date)	03/01/2020 - 12/31/2023 (with NCE to 12/23)
Reporting Period	03/01/2020 - 12/31/2023
Report Term or Frequency	Final
Signature of Submitting Official	 Jason C. Hicks

2. DISCLAIMER

3. ACKNOWLEDGMENT

This material is based upon work supported by the Department of Energy under Award Number DE-FE0031862.

4. TABLE OF CONTENTS

5. EXECUTIVE SUMMARY

The US relies heavily on domestic natural gas production and processing for residential, commercial and industrial energy needs. Natural gas consists primarily of light hydrocarbons (e.g., methane, ethane) that are used directly as fuels or converted into other chemicals. Due to the reliance on natural gas, it is important that the operations used to collect and process this valuable component are efficient and effective. Natural gas can be produced in stranded locations that are not connected to pipelines, which makes transportation of the gas difficult and flaring or venting of the gas more feasible.

In this project, we present a plasma-assisted, catalytic process that can handle variations in production rates and gas compositions of producing wells and reliably converts the hydrocarbons to gas phase olefins, high molecular weight alkanes, and liquid chemicals. The low-temperature plasma serves as a reactive chemical environment that activates and converts the light hydrocarbons to these valuable products. We present results from the integration of a catalyst into the low-temperature plasma zone to improve reaction efficiency and product selectivity. We show that the gas composition, bulk gas temperature, and input power of the plasma, with and without catalysts, influence the production rates of liquids from natural gas feeds.

Overall, we have designed, developed, and tested a process for direct light hydrocarbons-to-liquids conversion via plasma-assisted, catalytic chemistry. The results from this project could have a profound impact on the current processing of natural gas by opening up new avenues to producing valuable N-containing chemicals useful in products such as pharmaceuticals. The proposed research is directly in line with the goals and approach of the FOA (DoE/NETL). This final project report is responsive to the requirements in the Department of Energy (DOE), Office of Fossil Energy (FE), Advanced Natural Gas Infrastructure Technology Development Funding Opportunity Announcement (FOA) DE-FOA-0002006.

6. PROJECT OVERVIEW

Flaring light hydrocarbons from wells and refineries amounts to a global, annual loss of >140 billion m^3 of natural gas. Not only are valuable, non-renewable hydrocarbons misused during this process, but flaring also contributes more than 400 metric tons of CO_2 to the environment. The implementation of chemical processing technology that directly converts light gases to liquid products will relieve the strain associated with gas separations and gas compression at the source. Further, the development and discovery of new strategies or processes to convert natural gas (and specifically methane) directly to liquid chemicals has received a considerable amount of attention.

The goal of this project is to use plasma stimulation of a light hydrocarbon resource to synthesize value-added liquid chemicals. This work will evaluate the hypothesis that the plasma will serve multiple roles in this transformative chemistry including: (1) activation of Carbon - Hydrogen (C-H) bonds at low bulk gas temperature and pressure, (2) providing a fast response for immediate startup and shutdown, (3) enhancing the lifetime of the catalyst through plasma-assisted removal of surface impurities, and (4) providing a means to activate Nitrogen (N_2) to allow for the direct formation of chemicals containing nitrogen–carbon (N-C) bonds. In addition, the project will explore the potential for exploiting these processes more broadly, by building on recent discoveries using plasma-assisted methods to convert hydrogen and N_2 feeds.

In this project, we couple N_2 activation and C-H activation together in a plasma-assisted, catalytic reaction system to produce high value chemicals at near-ambient conditions. Due to the ubiquitous occurrence of N-containing compounds in nature, the formation of heterocyclic aromatic compounds (e.g., pyrrole, pyridine etc.) is important in the synthesis of natural compounds, medicinal chemistry, specialty chemicals/pharmaceuticals, and green solvents such as ionic liquids. We perform these non-trivial reactions starting with molecular N_2 and light hydrocarbons (CH_4, C_2H_6, C_3H_8, or gas mixtures) to produce N-containing aromatic species. We were motivated by preliminary results that provide evidence that plasma-catalyst combinations perform N-C coupling starting from molecular N_2 and an alkane. Therefore, our target was to produce N-containing hydrocarbon species that are difficult to produce via conventional catalytic approaches.

7. PROJECT TEAM

The project team consists of four faculty members located at the University of Notre Dame. Prof. Jason Hicks (Principal Investigator, University of Notre Dame) has expertise in catalyst synthesis/characterization and in the design, construction, and operation of plasma catalysis reactors. He was responsible for tasks related to performance evaluation in the plasma reactors and served as the ND Project Lead. Prof. David Go (co-PI, University of Notre Dame) has expertise in the development and characterization of low-temperature, non-equilibrium plasma systems, including the design of plasma catalysis reactors. He was responsible for tasks related to plasma reactor development, plasma characterization, and evaluation of reactor performance, working closely with PI Hicks. Prof. Casey O'Brien (co-PI, University of Notre Dame) has expertise in the mechanistic evaluation of catalytic materials using in-situ/operando spectroscopic characterization and systematically changing the structure and composition of catalysts to obtain

detailed structure-function relationships. Prof. O'Brien was responsible for the development of an in situ/operando technique to study plasma-catalyst interactions. Prof. William Schneider (co-PI, University of Notre Dame) has expertise in the computational modeling of surface catalytic reaction mechanisms and rates and of plasma-surface catalysis interactions. He was responsible for tasks related to catalyst property prediction and models for optimizing plasma-catalyst integration.

8. ACCOMPLISHMENTS:

List of Accomplishments:

- Four new reactors were constructed and validated at the University of Notre Dame.
- The PIs developed a plasma-assisted process to facilitate methane activation/coupling and liquid production by combining reaction performance results, in situ/operando characterization, and predictive modeling.
- The project team identified process conditions and gas compositions that promote production of liquids from plasma stimulation.
- The project team successfully incorporated catalysts into the plasma environment to enhance the liquid yields.
- An in situ/operando spectroscopy tool has been developed to simultaneously probe the plasma phase and catalyst surface under plasma exposure.
- Training/Professional Development: 7 students and 2 postdocs supported by this grant, students trained on campus facilities (e.g., NMR, CHN analysis, reactor design/development, plasma systems, IR…), attended machine learning workshop, attended NACS NAM 2023, AIChE 2020-2023, ACS 22-23, and Gaseous Electronics Conference meetings
- Two patent applications were filed.
- Eight manuscripts published to date.

9. MILESTONE LOG

Table 1. Milestone log including completion dates and milestones in progress.

Subtask	Milestone Title & Description	Planned Completion Date	Actual Completion Date	Verification Method
1.1	Update the Project Management Plan	03/31/2020	2/21/2020	Submission to DOE Project Officer
1.2	Provide Technology Maturation Plan	04/30/2020	04/14/2020	Submission to FITS@NETL.DOE.GOV
1.3	Provide preliminary Technoeconomic Evaluation	08/28/2020	08/26/2020 (to DOE project officer)	Submission to DOE Project Officer

			09/28/2020 (to FITS@NETL.DOE.GOV)	
2.1, 2.2	Demonstrate, through the collection and identification of products, a DBD reactor producing N-containing liquids from light hydrocarbon feeds	11/30/2020	11/30/2020	Documented and disclosed experimental evidence within quarterly research performance progress report.
2.3	Electrical characterization (current, voltage, and charge data) of the plasma reactor for different variations in plasma power (1-15 W), flow and temperature conditions (298 – 1000 K, 20 – 200 ml/min, CH_4/N_2 = 0.05 - 10 ratios, C_2H_6/N_2 = 0.05 – 10)	11/30/2020	11/30/2020	Documented and disclosed experimental evidence within quarterly research performance progress report.
2.4	Detection of surface-adsorbed species in the presence of a plasma jet using polarization modulation infrared-reflection absorption spectroscopy under the following conditions: ($P_{hydrocarbon}/P_{N2}$ = 0.05 – 10), plasma power (1-5 W), temperature (298-600 K)	02/28/2021	11/30/2020	Documented and disclosed experimental evidence within quarterly research performance progress report.
3.1, 3.2	Determine production rates of N-containing products from plasma stimulation and compare these to thermal (non-plasma stimulation) production rates, identifying all conditions that exceed the thermal process.	08/31/2021	07/16/2021	Documented and disclosed experimental evidence within quarterly research performance progress report.
3.3	Plasma reactor evaluated through product selectivity for O_2 and CO_2 limits at various compositions (0-1% O_2 or 0-50% CO_2 in feed).	11/30/2021	8/1/2021	Documented and disclosed experimental evidence within quarterly research performance progress report.
2.5, 3.6	Model that relates operating conditions to reactor performance exists, is parameterized against available data, and makes predictions outside known condition space. Model success evaluated through comparison of predicted and observed response of system to changes in operating parameters.	11/30/2021	10/8/2021	Documented and disclosed computational models described within quarterly research performance progress report.

4.2	Complete optical characterization of hydrocarbon:N_2 plasma and identify relative spectral intensities of C-H (314 nm), C2 (512, 516, and 558 nm), and NH* (336 nm) species	11/30/2021	11/30/2021	Documented and disclosed experimental evidence within quarterly research performance progress report.
5.1, 5.2, 5.3	Selective N-C forming catalysts experimentally identified by evaluating the selectivity to products of zeolite and metal-based catalysts	08/31/2022	4/30/2022	Documented and disclosed experimental evidence within quarterly research performance progress report.
5.5	Chemistry-specific model is developed and predicts changes in selectivity with changes in material. Model evaluated through comparison of predicted and observed responses to changes in material.	11/30/2022	11/30/2022	Documented and disclosed computational models described within quarterly research performance progress report.
5.4	Spectroscopic identification of plasma-surface interactions for N-C formation	02/28/2023	02/28/2023	Documented and disclosed experimental evidence within quarterly research performance progress report.
4.3	Operation of alternative plasma reactor configuration and characterization of power consumption and electrical characteristics (current and voltage) under different flow and temperature conditions	11/30/2022	11/30/2022	Documented and disclosed experimental evidence within quarterly research performance progress report.
6.1, 6.2	Optimal plasma reactor configuration identified and demonstrated through the operation of ~1 scfm (TRL 4) plasma/reactor system	02/28/2023	12/30/2023	Documented and disclosed experimental evidence within quarterly research performance progress report.

10. TECHNICAL PROGRESS

Project Management and Planning (Subtasks 1.1, 1.2, and 1.3)

As part of the requirements of the proposed work, we updated the Project Management Plan (PMP) within 30 days after award and as necessary throughout the project to accurately reflect the status of the project. The PMP was updated prior to the start of the project on 2/21/2020.

We developed a Technology Maturation Plan (TMP) that described the current technology readiness level (TRL) of the proposed technology/technologies, related the proposed project work

to maturation of the proposed technology, and described known post-project work necessary to further increase the technology TRL level. The TMP was submitted on 4/14/2020.

We developed and provided NETL a preliminary Techno-Economic Assessment (TEA) for the proposed technology on 8/26/2020. The TEA was updated as the research progressed, and a final TEA was submitted 12/2023. The Final TEA is provided as an appendix to this document.

Plasma Catalysis Reactor Construction and Performance Evaluation (Subtasks 2.1, 2.2, 2.5, 3.1, 3.2, and 3.6)

In preliminary experiments containing hydrocarbons and nitrogen under plasma stimulation, a dark colored liquid product formed and coated the walls of the reactor. Because this liquid was of interest to the project, a new reactor design was proposed to include a liquid collection vessel downstream from the reactor zone for improved collection efficiency (Figure 1). The reactor was connected to a downstream GC and in-line MS for gas phase analysis. The liquid collected was analyzed by 1H NMR, 13C NMR, FT-IR, ESI-MS, and elemental analysis.

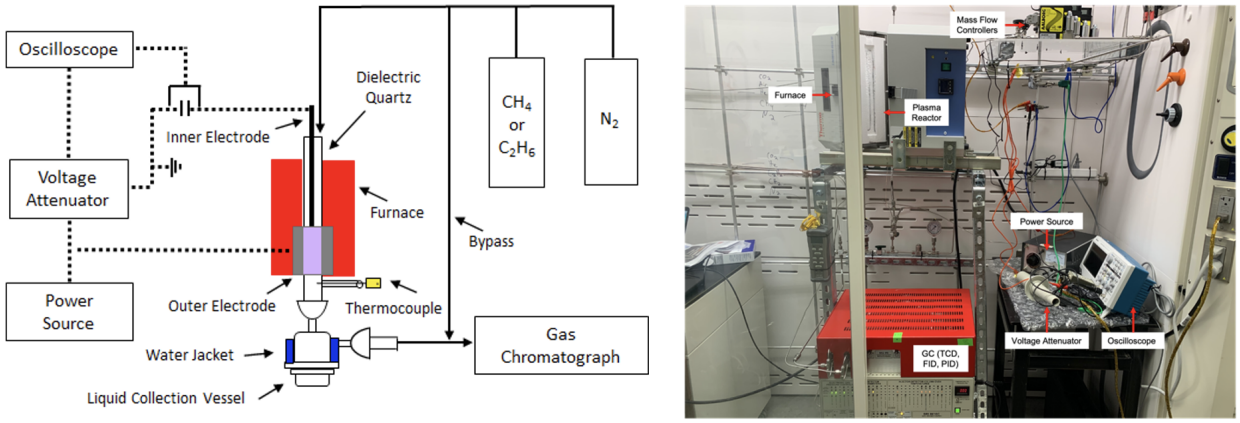

Figure 1. Plasma reactor system.

The reactor was tested and validated using either a methane/nitrogen feed or an ethane/nitrogen feed. The residence time, composition, bulk gas temperature, and plasma power were individually varied in order to map out the reaction conditions that promote gas and liquid phase products.

The effect of residence time on the methane consumption rate was studied at 10 W input power and 200°C. As shown in Figure 2, the CH_4 consumption rate decreases with an increase in residence time. The inverse is observed for methane conversion, where conversion increases as the residence time increases. In terms of the product distribution, ethane, ethylene, acetylene and propane were detected.

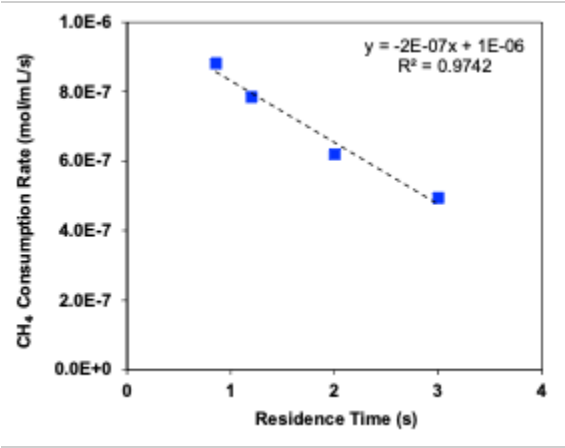

Figure 2. (a) CH_4 consumption rate as a function of residence time.

The gas composition was varied between 5-80% methane with the balance N_2. As seen in Figure 3, the ethane consumption rate increases as the concentration of methane increases in the feed. Experiments with 50% or more nitrogen produced a liquid product stream in addition to the gas phase products. The experiments containing 80% methane and 20% nitrogen produced gases and solid carbon deposits in the reactor.

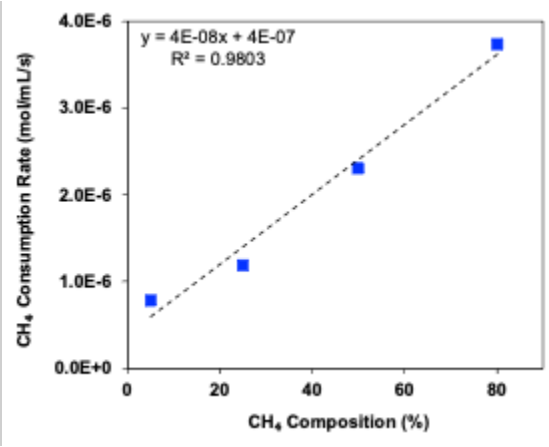

Figure 3. Methane consumption rate as a function of gas composition.

The plasma power was varied for both methane and ethane feed streams (Figure 4). Figure 4 shows that as the input power is increased, both the methane and ethane consumption rates increase. Liquids were observed during reactions operated at 7 and 10 W, but higher power inputs resulted in more carbon deposition and no liquid products. Lower powers likely produce liquids as well, but the conversions were lower and less products were observed.

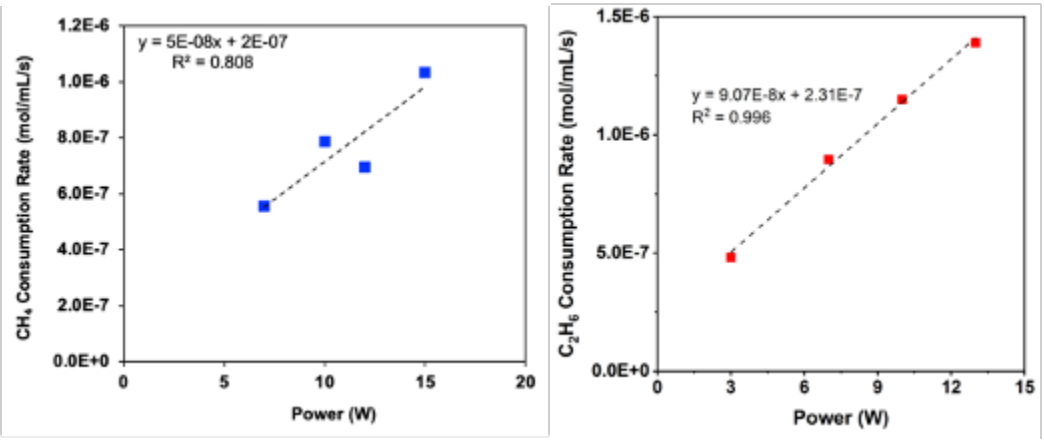

Figure 4. Plots of methane consumption rate (left) vs. power and ethane consumption rates (right) vs. power.

As shown in Figure 5, the ethane conversion decreases as temperature increases for a plasma stimulated ethane feed. Reactions of methane as a function of temperature result in very similar results, where conversion approaches 0 as the temperature is increased above 300 oC. For the ethane reactions, the ethylene yields decrease at higher temperatures (> 200 ºC). The liquid production rate remains higher at the lower temperatures, and decreases at higher temperatures as the ethane conversion drops.

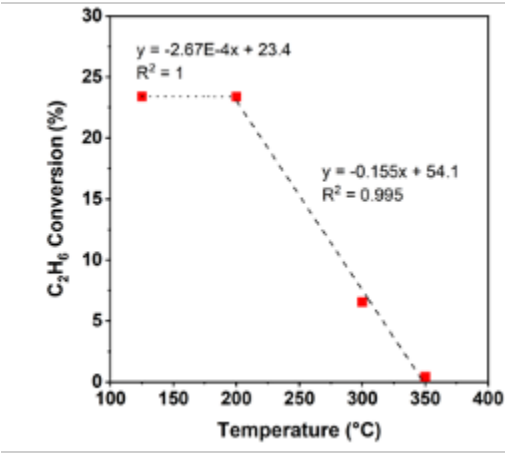

Figure 5. Ethane conversion as a function of temperature.

A simulated Bakken shale gas stream was tested to determine the effects of a mixed hydrocarbon feed under plasma stimulation. A reaction was performed at 10 W, 50 ml/min, and 200 °C, matching the composition of the Bakken as close as possible with the limitations of the mass flow controllers ($CH_4/C_2H_6/C_3H_8/N_2$ = 1/0.31/0.18/0.13). No liquids were observed at this composition, which is consistent with experiments performed with only CH_4 or C_2H_6 and similar amounts of N_2. The nitrogen content in the feed was then varied while keeping the hydrocarbon ratios and total flow rate constant. Figure 6a shows that as the amount of nitrogen in the feed increases

(corresponding to a decrease of hydrocarbons in the feed), the hydrocarbon consumption rates decrease, while the nitrogen consumption rate increases. This matches well with the hydrocarbon and ammonia production rates shown in Figure 6b.

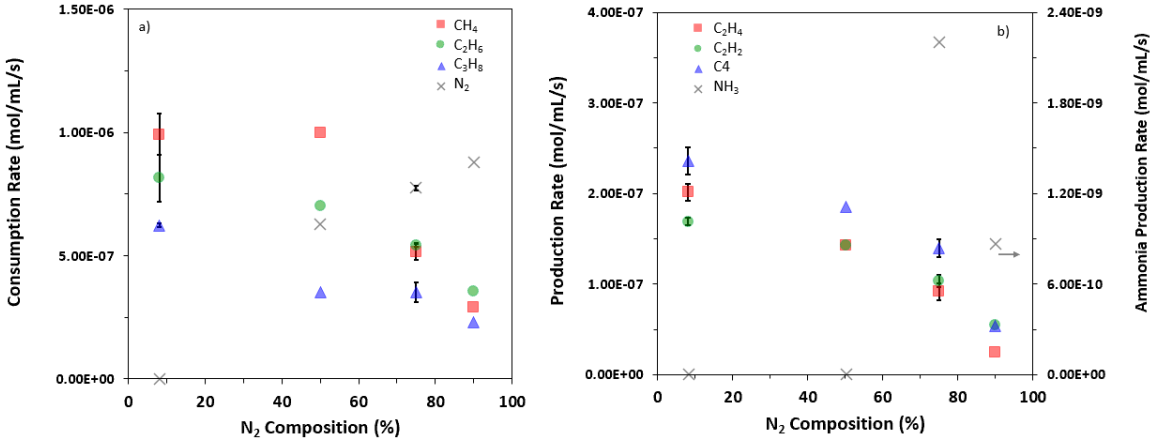

Figure 6. a) Hydrocarbon and nitrogen consumption rates and b) hydrocarbon and ammonia production rates for the simulated Bakken feed with varying nitrogen feed composition. Reactions were done at 10 W, 200 °C, and 50 ml/min.

As more nitrogen was added to the feed, the amount of liquid production increased, as seen in Figure 7. The decrease in the carbon balance can be accounted for by the liquid formation. At low nitrogen feed compositions, when no liquid is formed, a good carbon balance can be achieved as most gas phase products can be quantified using a GC. As more liquid is produced, the gas phase products only account for part of the carbon balance.

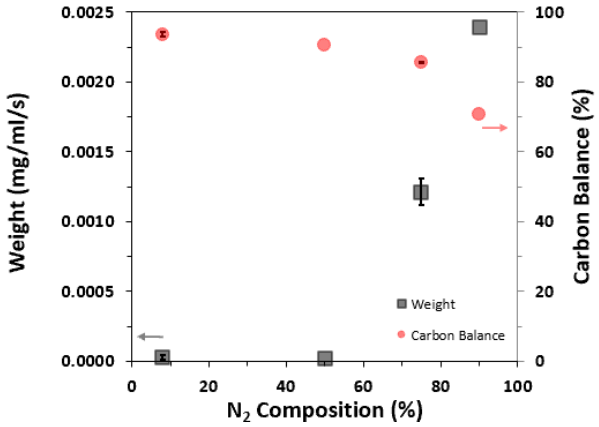

Figure 7. Liquid production rates and carbon balances for the simulated Bakken feed with varying nitrogen feed composition. Reactions were done at 10 W, 200 °C, and 50 ml/min.

We used MALDI-TOF-MS to analyze the liquid samples collected after reaction of a mixed shale feed enriched with 90% N_2. The spectrum in Figure 8 shows evidence of chain growth; specifically, additions of 14 m/z can indicate -CH_2- chain growth or the addition of a nitrogen, and 27 m/z can be the oligomerization of HCN. The stability of the product was analyzed by

performing MALDI analysis on three consecutive days. The peaks at lower m/z begin to disappear over the 3-day period, indicating that these lower molecular weight species evaporate with time. This emphasizes the importance of analyzing the liquid product soon after reaction. However, the higher molecular weight compounds appear to be stable over time.

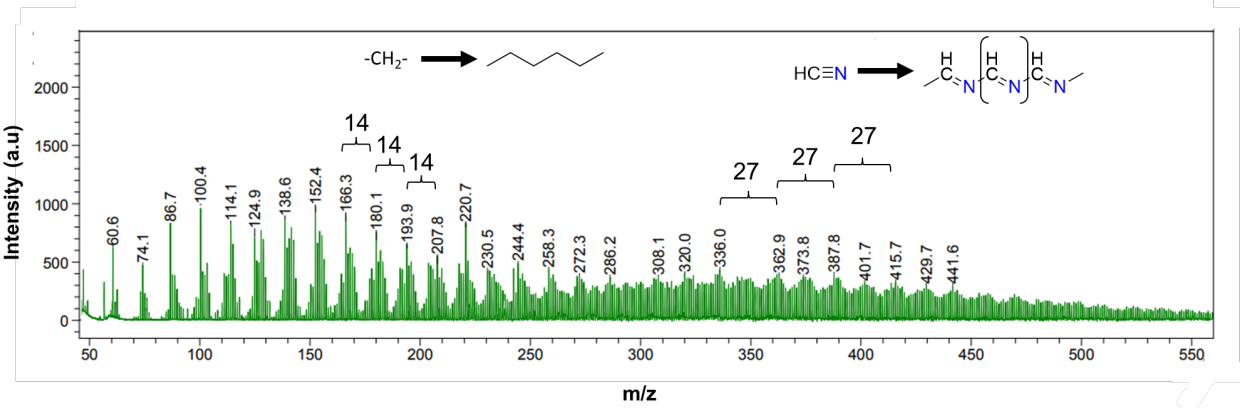

Figure 8. MALDI-TOF-MS spectra of the liquid produced after reaction of the mixed shale feed enriched with 90% N_2. Evidence of polymeric chain growth is seen.

Taken together, we identified operating conditions that improved liquid formation and conditions that favored valuable gas formation (e.g., olefins, C3+ species). As evidenced from these experiments, higher concentrations of nitrogen in the feed promoted N-C coupling events and thus liquid formation. Additionally, pure feeds were not required, as the simulated Bakken well showed similar upgrading to both olefins and liquid products.

Improving Selectivity to Liquids via Plasma-Assisted Catalysis (Subtasks 5.1 and 5.2)

From experiments discussed in the previous section, it is evident that the selectivity is not easily controlled using a plasma-only approach. In an effort to shift the selectivity to liquid products, we incorporated catalysts within the plasma reaction zone. Specifically, we incorporated Mo/HZSM-5, which is known to perform thermal methane dehydroaromatization chemistry, in the non-thermal plasma reactor with a feed stream containing a CH_4/N_2 reaction mixture. We evaluated the catalyst at different bulk gas temperatures in the presence of a DBD plasma.

Figure 9 shows CH_4 conversion as a function of temperature for two different reaction environments: DBD-only and DBD-Mo/HZSM-5. For the DBD-only system, where no catalyst is present, we observe that as the temperature is increased, the initial CH_4 conversion decreases and approaches zero, which was also observed for ethane experiments showcased in Figure 5 above. However, in the presence of Mo/HZSM-5, a higher conversion is observed over the DBD-only experiments at temperatures of 500 °C and higher. In addition, for the plasma-catalytic system, a shift in the product distribution to aromatics is observed, as shown in Figure 10. As the temperature is further increased in these reactions, the selectivity toward benzene increases.

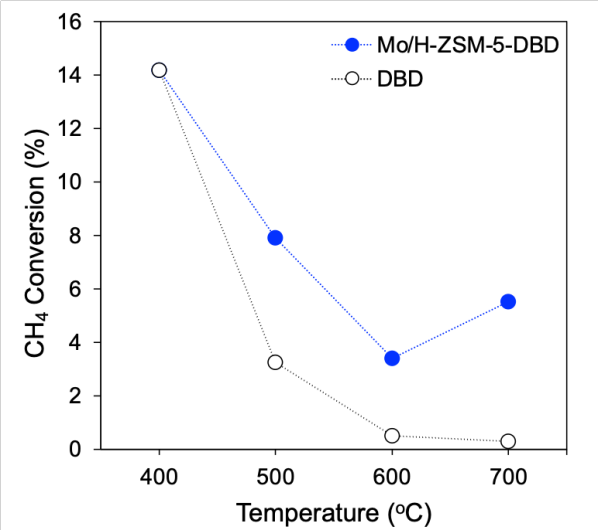

Figure 9. CH_4 conversion as a function of reaction temperature for a plasma-only and plasma-catalytic system. Reaction conditions consisted of a 50% CH_4 in N_2 feed, plasma power input of 10 W, frequency of 20 kHz, a total flow rate of 50 sccm at ambient pressure.

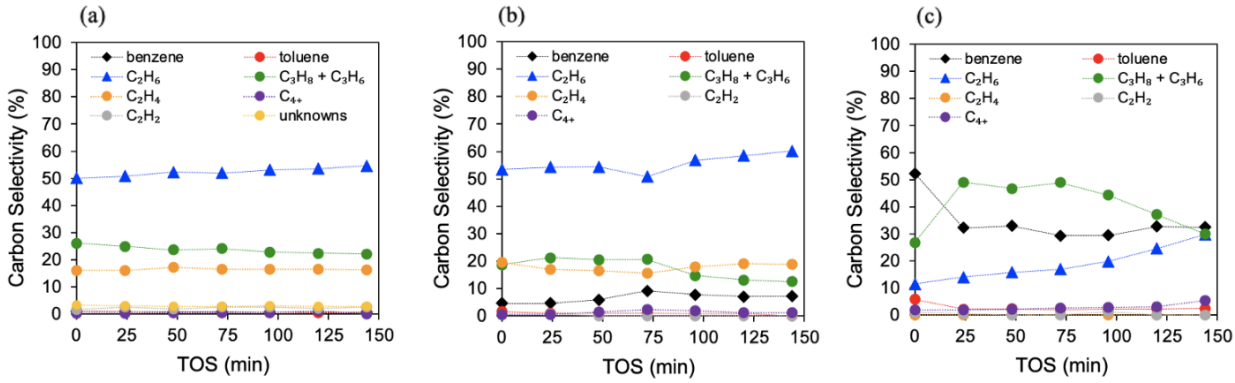

Figure 10. Product distributions obtained for the plasma-catalytic system for (a) 400 °C, (b) 500 °C, (c) 600 °C.

More recently, we have been able to show that the synthesis of molybdenum carbide, which is argued to be the active site toward C-H activation, can be facilitated by plasma stimulation of a CH_4 feed at lower temperatures. Typically, molybdenum carbide can be synthesized through a temperature-programmed reduction of molybdenum oxide exposed to a mixture of hydrogen and carbon-containing gases. Figure 11 shows an XRD pattern for molybdenum carbide phases supported on amorphous silica synthesized from MoO_3 with a 10 W plasma treatment at 500 °C. This result indicates that a DBD plasma can assist in the conversion of molybdenum oxide to molybdenum carbide phases at 500 °C (and as low as 300 °C from XPS studies), whereas the thermal treatment at this condition is not able to form a MoC_x phase.

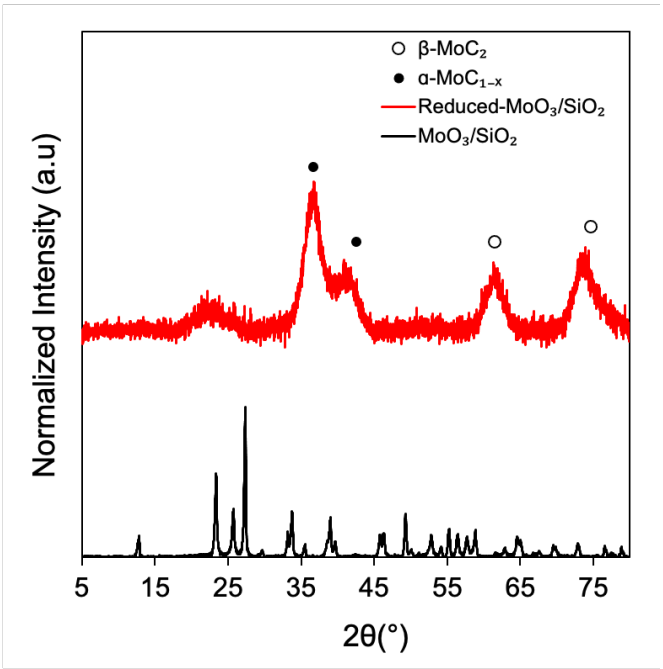

Figure 11. XRD patterns of molybdenum carbide prepared by plasma treatment at 500 ºC under a 50% CH_4 feed in N_2.

Overall, selectivity to liquid aromatics was significantly improved and catalyst synthesis was possible at lower bulk gas temperatures under plasma stimulation compared to thermal routes. The need for Mo is not necessary, as HZSM-5 performed similarly at lower temperatures. In separate experiments, other metal additives (i.e., Ga) resulted in better aromatic selectivity than Mo and may be candidates for this reaction.

We developed a microkinetic model to describe the coupling of methane and nitrogen on a catalyst surface. The model was based upon literature results for the thermal CH_4 + NH_3 chemistry (Gómez-Díaz *et al. J. Phys. Chem. C* 2011, 115, 13, 5667–5674) and implemented and exercised for plasma-excited CH_4 and N_2, to look for CH_3CN products. Comparisons of model results with experiments indicate that the model was missing critical elements of the experiment and would not be useful for materials selection.

<u>Design of In Situ/Operando Plasma IR System and In Situ Observation and Modeling of Plasma-Surface Interactions (Subtasks 2.4, 2.5, 3.5, 3.6, 6.1)</u>

Design of In Situ/Operando Plasma IR System and In Situ Observation

To investigate the interaction between non-thermal plasma-activated CH_4 and N_2 species and a model surface, a multi-modal spectroscopic tool was designed. The multi-modal spectroscopic tool combines polarization-modulation infrared reflection-absorption spectroscopy (PM-IRAS), optical emission spectroscopy (OES), and mass spectrometry (MS) to monitor surface-adsorbed, plasma-phase, and gas-phase species, respectively (Figure 12). The design is based on the

modification of a commercially available Harrick Refractor Reactor (spectroscopic cell). The lid of the spectroscopic cell is modified to implement (1) a flared quartz tube for alternating current (AC) dielectric barrier discharge (DBD) plasma jet, (2) an optical window for OES, and (3) MS capillary.

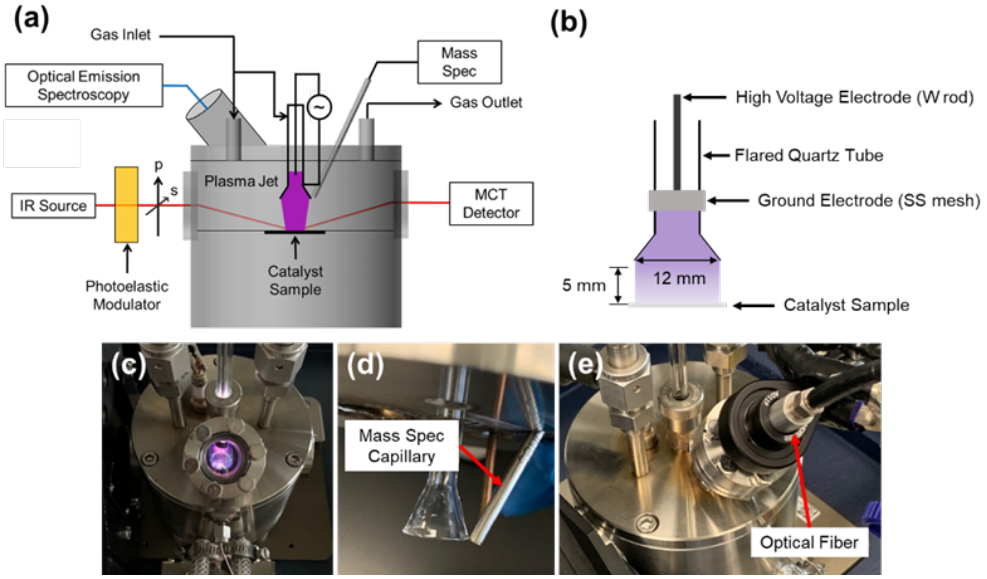

Figure 12. (a) schematic of multi-modal spectroscopic cell, (b) schematic of DBD plasma jet with a flared quartz tube, (c) photograph of the setup under operation, (d) photograph of mass spectrometry (MS) capillary, and (e) photograph of optical fiber for OES.

To minimize the plasma-phase interactions between plasma-activated CH_4 and N_2 species, the two simplest systems (i.e., CH_4- and N_2-only systems) were first investigated then the complexity of the system was increased stepwise (sequential exposure, then simultaneous exposure of CH_4 and N_2) using the multi-modal spectroscopic tool.

First, the interaction between plasma-activated CH_4 and Ni and SiO_2 surfaces was investigated in two separate steps, namely the deposition and activation steps. During the deposition step, the surfaces were exposed to an Ar plasma jet (7kV peak-to-peak; 100 mL/min) into CH_4 surrounding gas (25 mL/min) at 25 °C and 1 atm. After the deposition step, the system was purged with inert Ar gas to remove residual CH_4. Then, subsequently, the surfaces were exposed to an Ar plasma jet (3.3 kV peak-to-peak; 100 mL/min) at 25 °C and 1 atm for the activation of surface-deposited species.

Figure 13 compares the PM-IRAS spectra of (a) Ni and (b) SiO_2 during the deposition step. In-situ PM-IRAS observation of Ni and SiO_2 surface reveals the surface-dependent deposition during CH_4 exposure in the presence of an Ar plasma jet. On Ni, the growth of CH_x (1300-1500 and 2800-3000 cm^{-1}) containing species was detected upon application of the Ar plasma jet (7 kV, peak-to-peak). On SiO_2, however, a much weaker CH_x (2800-3000 cm^{-1}) feature was observed. Simultaneous in-situ OES shows the same plasma radical species were present with both Ni and

SiO_2 during the deposition step (Figure 14). The similarity in the plasma-phase properties and the differences observed on the surface suggest that transition metal Ni is more interactive with plasma radicals to form carbonaceous deposits than SiO_2.

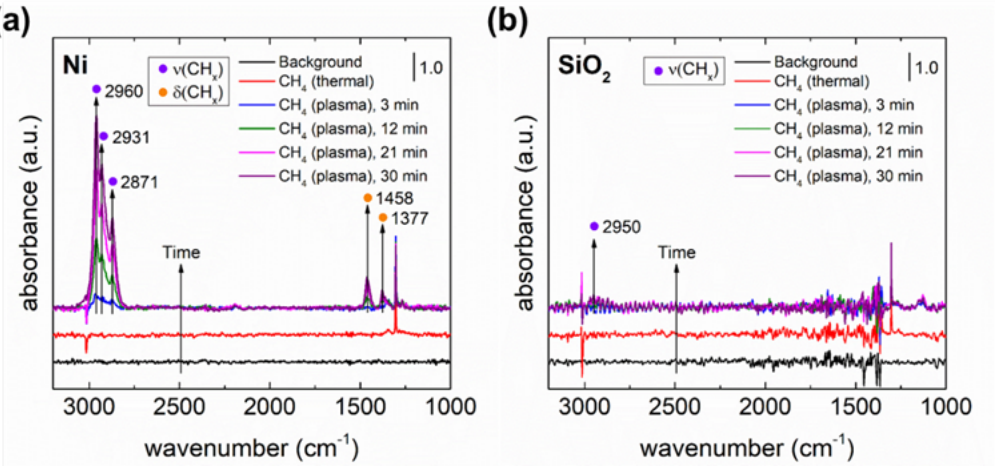

Figure 13. PM-IRAS spectra of adsorbed species on (a) Ni and (b) SiO_2 during the deposition step using an Ar plasma jet at ~20 kHz and 7 kV (peak-to-peak) into a CH_4 atmosphere at 25 °C and 1 atm for 30 min. Black spectra are the background spectra obtained under 100 mL/min of pure Ar flow. Red spectra obtained after the introduction of 25 mL/min CH_4, prior to plasma jet ignition.

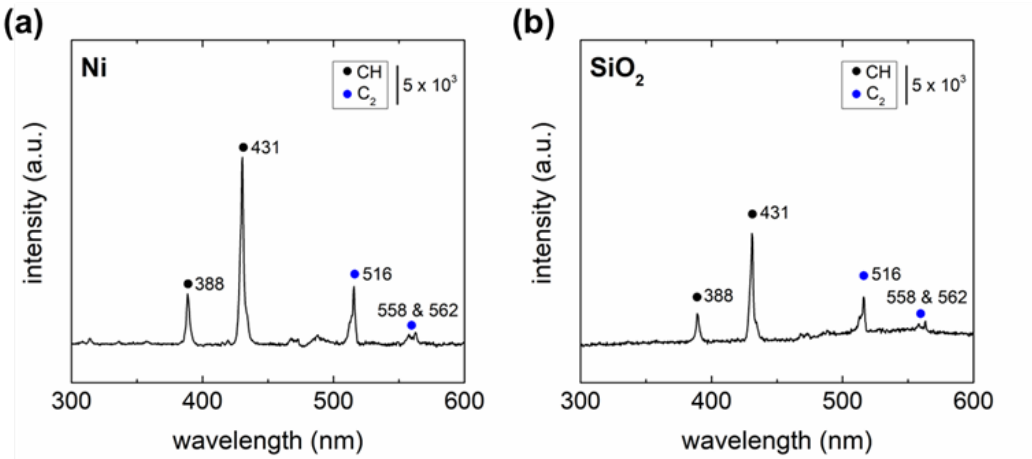

Figure 14. OES spectra for (a) Ni and (b) SiO_2 samples during the deposition step using an Ar plasma jet at ~20 kHz and 7 kV (peak-to-peak) into a CH_4 atmosphere at 25 °C and 1 atm.

Figure 15 shows the PM-IRAS spectra of (a) Ni and (b) SiO_2 during the activation step. Application of the Ar plasma jet into the purged system caused the peaks assigned to CH_x to decrease while a broad peak centered at 1691 cm^{-1} (C=C containing species) appeared on Ni. On the other hand, the formation of C=C was not observed on SiO_2. However, the corresponding MS signal during the activation step (Figure 16) shows an increase in H_2 (m/z = 2) and C_2 hydrocarbons (m/z = 26 and 28, corresponding to C_2 hydrocarbons including acetylene, ethylene, and ethane) was observed on Ni and SiO_2. From the OES measurement (Figure 17) during the activation step,

it is shown that with the Ni surface, no peaks associated with plasma radical species were observed, while with the SiO_2 surface, CH radical species were observed. These results suggest that the formation of surface C=C and H_2 and C_2 hydrocarbons during the activation step is most likely a surface phenomenon on Ni but a plasma-phase phenomenon with SiO_2.

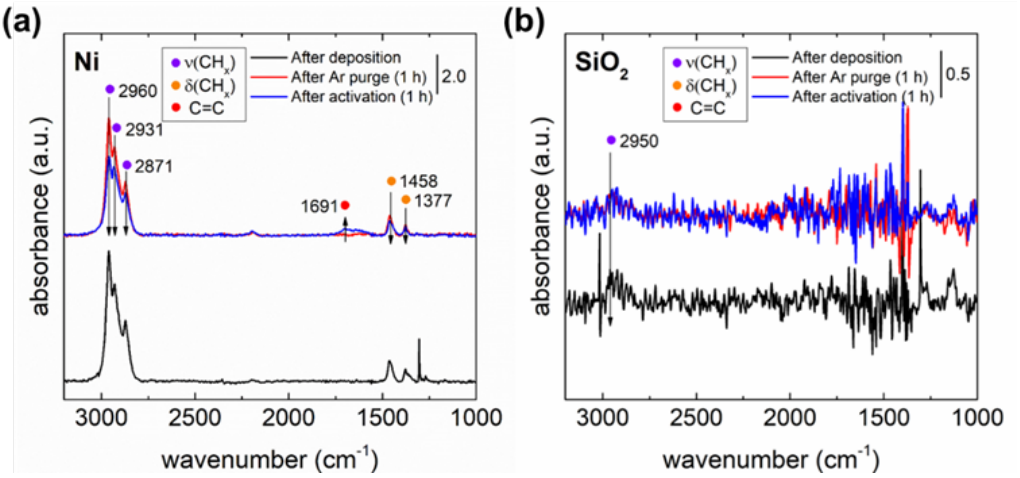

Figure 15. PM-IRAS spectra on (a) Ni and (b) SiO_2 during the activation of carbonaceous deposits using an Ar plasma jet at ~20 kHz and 3.3 kV (peak-to-peak) at 25 °C and 1 atm for 1 hour. Black spectra show the surface adsorbed species after the initial deposition. Red spectra were obtained after 1 hour of purge to remove CH_4 from the system, prior to Ar plasma jet introduction.

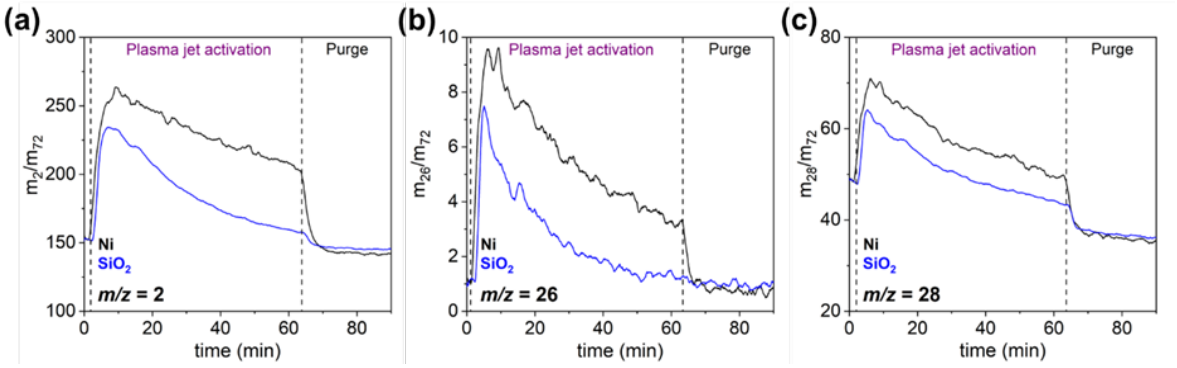

Figure 16. Gas-phase products (a) H_2 (*m/z = 2*), (b) acetylene, ethylene, or ethane (*m/z = 26*), and (c) ethylene, ethane, or acetylene (*m/z = 28*) monitored during the activation step using an Ar plasma jet at ~20 kHz and 3.3 kV (peak-to-peak) at 25 °C and 1 atm for 1 hour. Black lines are MS signals with Ni. Blue lines are MS signals with SiO_2. MS signals are divided by mass to charge of pentane (m/z = 72) to compare the amount of gas-phase products in both experiments.

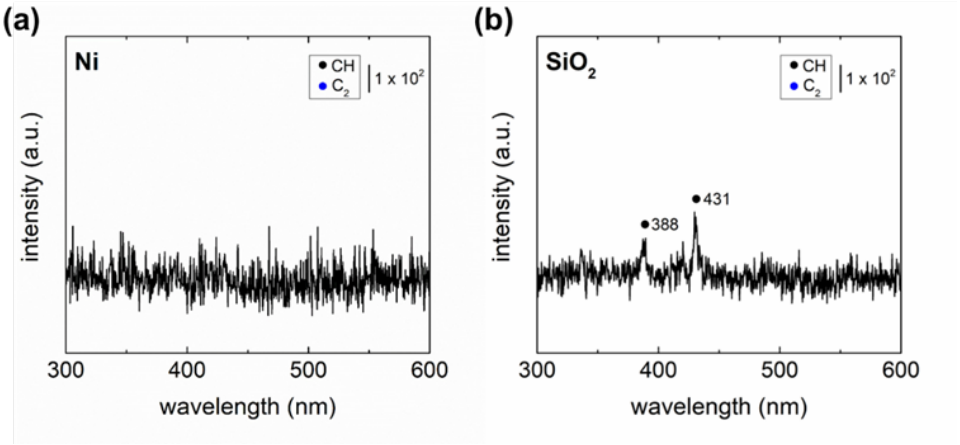

Figure 17. OES spectra of Ar plasma jet during the activation step with (a) Ni and (b) SiO_2. Ar plasma jet is operated at ~20 kHz and 3.3 kV (peak-to-peak).

Then, the interaction between plasma-activated N_2 and five different metal surfaces (Ni, Pd, Cu, Ag, and Au) was investigated. Metal surfaces were exposed to an Ar plasma jet (7 kV peak-to-peak; 60 mL/min) into N_2 surrounding gas (40 mL/min) at 25 °C and 1 atm. From the interaction, on every metal surface, the formation of thermally stable ~2200 cm^{-1} PM-IRAS feature was observed during the plasma exposure (Figure 18). For example, the surface temperature of Ni has to be higher than ~165 °C to desorb the adsorbed species responsible for the ~2200 cm^{-1} PM-IRAS feature.

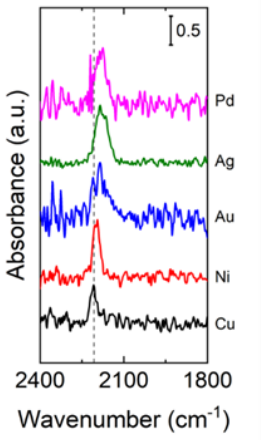

Metal	Average Peak Position with 95 % Confidence Interval (cm^{-1})
Ni	2196 ± 6
Pd	2177 ± 14
Cu	2206 ± 6
Ag	2181 ± 19
Au	2182 ± 14

Figure 18. (Left) stacked normalized PM-IRAS spectra of adsorbed species on Cu, Ni, Au, Ag, and Pd during exposure with an Ar plasma jet at ~20 kHz and 7 kV (peak-to-peak) into a N_2 atmosphere at 25 °C and 1 atm for 3 min. (Right) average peak position with 95% confidence intervals from three replicates.

Density functional theory calculations were used to assess potential assignments of the features shown in Figure 18. Figure 19 reports a parity plot of observed vs computed vibrational features of four candidate surface intermediates. As evident from panels (a) and (c), neither adsorbed N2 nor CN could plausibly account for the feature. A good parity is found for adsorbed N_3, which

initially led us to assign the feature to this unusual intermediate. A correlation but not parity is observed for NCO.

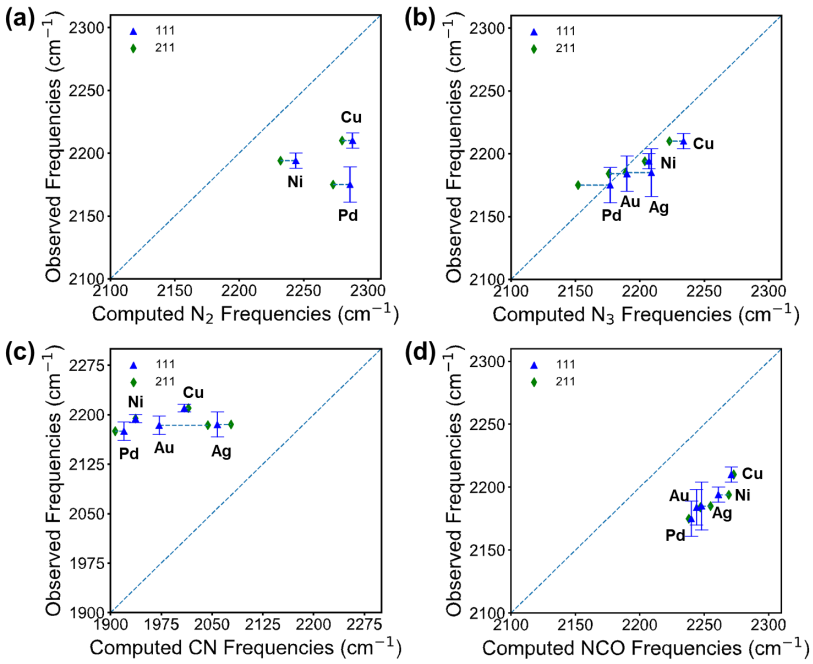

Figure 19. Parity plot of computed (a) N_2 frequencies, (b) N_3 frequencies, (c) CN frequencies, and (d) NCO frequencies over (111) and (211) surfaces with experimental observations under N_2 plasma irradiation. Horizontal dashed lines connect data of N_2, CN, N_3, and NCO on the same metal with different facets. Y-axis error bars represent the experimental 95% confidence interval from 3 replicates.

Identification of observed surface species was thoroughly investigated with isotopic labeling experiments with the Ni surface. When the Ni surface was exposed to isotopically labeled $^{15}N_2$ instead of N_2, the ~2200 cm^{-1} feature was shifted downward by ~10 cm^{-1} (Figure 20).

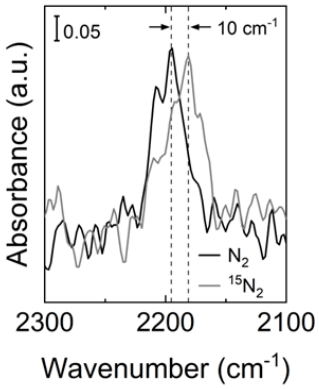

Figure 20. PM-IRAS spectra of Ni surfaces when the surfaces were exposed with Ar plasma jet into N_2 surrounding gas and $^{15}N_2$ surrounding gas at 80 °C and 1 atm. Two black dashed lines indicate the peak positions with N_2 and $^{15}N_2$.

We computed the expected isotopic shifts for the four candidate surface intermediates based on the original DFT results. $^{15}N_2$ and $^{15}N_3$ vibrational frequencies are expected to downshift ~70 cm^{-1} relative to their ^{14}N counterparts. The corresponding $C^{15}N$ and ^{15}NCO shifts are predicted to be ~30 cm^{-1} and ~10 cm^{-1}, respectively. Isotopic labeling thus supports assignment to NCO.

Then, NCO on the Ni surface was intentionally formed by (1) first adsorbing atomic N on the surface (N_{ads}), then (2) reacting N_{ads} with CO at 80 °C to form NCO on the surface. As shown in Figure 21a, intentionally produced NCO also exhibits the ~2200 cm^{-1} feature, supporting the isotopic-labeling results. NCO is also known to be reactive to H_2O. Thus, the reactivity of the ~2200 cm^{-1} feature formed with (1) N_2 plasma and (2) N_{ads} + CO towards H_2O was tested. Both features exhibited consistent behavior over time when they were exposed to H_2O, supporting that they are likely the same species (Figure 21b). Finally, the isotopic-labeling N_{ads} + CO experiment was performed with $^{15}N_2$ instead of N_2. The resulting PM-IRAS feature also showed a red-shift of ~10 cm^{-1}, supporting surface-adsorbed NCO (Figure 21a).

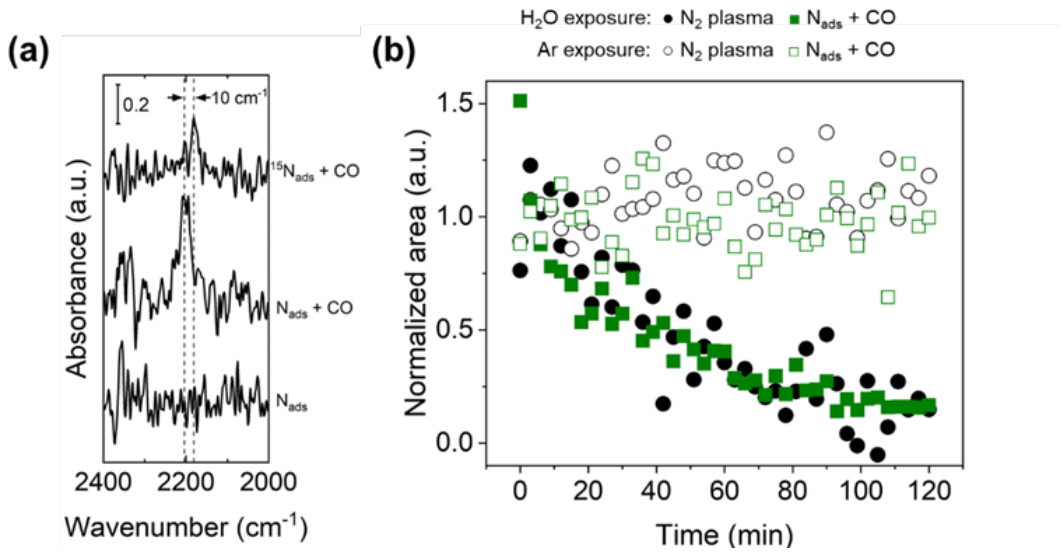

Figure 21. (a) PM-IRAS spectra of Ni surfaces that were treated with Ar plasma jet into N_2 at 200 °C and 1 atm to deposit N atoms on the Ni surface ('N_{ads}'), and then subsequently exposed to CO at 80 °C and 1 atm ('N_{ads} + CO'). The spectrum labeled '$^{15}N_{ads}$ + CO' was generated by first exposing Ni to $^{15}N_2$ plasma at 200 °C and 1 atm and then subsequently exposing the ^{15}N-covered surface to CO at 80 °C and 1 atm. The PM-IRAS spectrum was collected following CO exposure. Black dashed lines indicate the peak positions. (b) Normalized integral area of the PM-IRAS peak observed on Ni at ~2200 cm^{-1} during exposure to flowing Ar (open symbols) or humidified Ar (closed symbols) at 80 °C and 1 atm. The surface-adsorbed species with a characteristic PM-IRAS feature at ~2200 cm^{-1} was initially produced by exposure of Ni to N_2 plasma at 80 °C and 1 atm (black circles), or by first exposing Ni to N_2 plasma at 200 °C and 1 atm, to first deposit N atoms on the surface, followed by CO exposure at 80 °C and 1 atm (green squares). Each data point was normalized by the average of the first five data points to accommodate the variability due to the low PM-IRAS peak area.

Carbon and oxygen are believed to stem from ppm-level CO and CO_2 impurities in ultra-high purity (UHP) Ar and/or N_2 gas cylinders. These results indicate that even ppm-level impurities can affect the surface chemistry with plasma stimulation, and it needs to be considered more thoroughly in the investigation of plasma-catalytic surface interactions.

We used DFT calculations to contrast the energy landscapes for creating surface-bound N_3 and NCO on Ni terraces and steps (Figure 22). N_2 activation on Ni is computed to have significant activation barriers, consistent with the necessary intervention of plasma to drive development of surface N*. N_3* is predicted to be a metastable intermediate on Ni, upwards of 1 eV higher in energy than N* + N_2. N_3* is thus inaccessible thermally, and its formation, if observed, would have to come from additional plasma-driven routes, such as N* + excited N_2, of the sequential addition of two N radicals to N*. In contrast, formation of NCO* from adsorbed N* and CO is highly exothermic and is barrierless relative to the gas phase. CO* is also strongly bound to Ni itself. These model results are consistent with the preferential formation of NCO* over N_3*, in the presence of CO, and further suggests that NCO* forms only once available Ni sites are N* saturated, as CO itself prefers to bind to available Ni sites over N*.

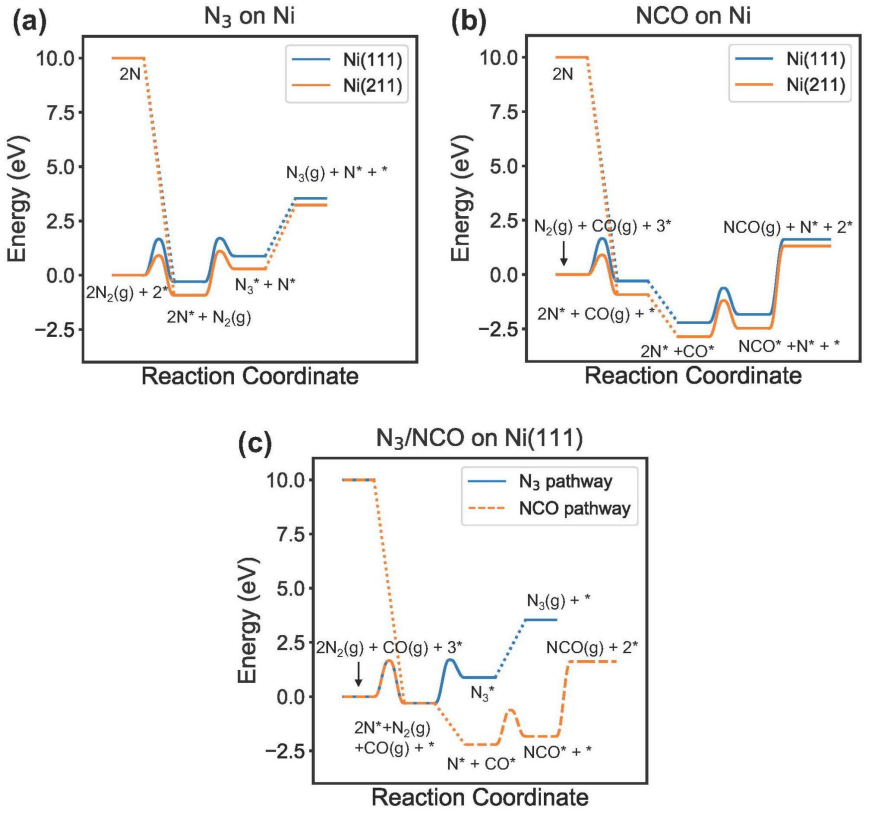

Figure 22. DFT-computed potential energy surfaces for formation of nitrogen-plasma-induced surface adsorbates: (a) N_3 on Ni; (b) NCO on Ni; (c) N_3 vs NCO on Ni.

After the study of CH_4- and N_2-only systems, sequential exposure of plasma-activated CH_4 and N_2 was investigated with five different metal surfaces (Ni, Pd, Cu, Ag, and Au) at 25 °C and 1 atm: (1) CH_4-N_2 sequence and (2) N_2-CH_4 sequence. As shown in Figure 23, when surfaces were first exposed to plasma-activated CH_4, the growth of CH_x-containing species was observed on every surface. Subsequent plasma-activated N_2 species exposure resulted in the appearance of PM-IRAS features in 1500~1700 cm^{-1} (C=N and C=C) and 2000~2200 cm^{-1} **(C≡N and C≡C) regions at the expense of CH_x** features in 1300~1500 cm^{-1} (bending) and 2800~3000 cm^{-1} (stretching). Optical emission spectra during subsequent N_2 exposure with plasma stimulation (Figure 24) exhibit a strong presence of CN violet band in the plasma phase.

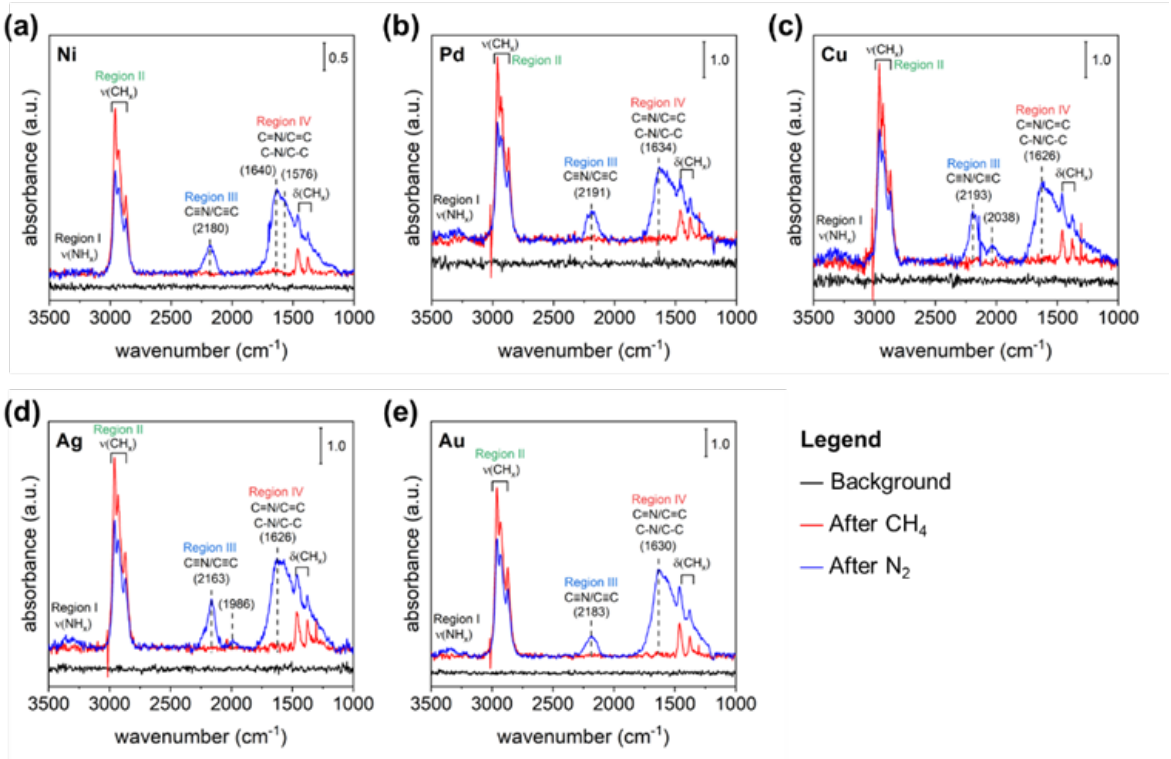

Figure 23. PM-IRAS spectra of adsorbed species on (a) Ni, (b) Pd, (c) Cu, (d) Ag, and (e) Au at 25 °C in sequential CH_4-N_2 exposure (red: after 30 minutes CH_4 exposure & blue: after subsequent 30 minutes of N_2 exposure). Surfaces were treated with an Ar plasma jet at ~20 kHz and 7 kV (peak-to-peak) into either CH_4 or N_2 atmosphere at 1 atm for 30 min.

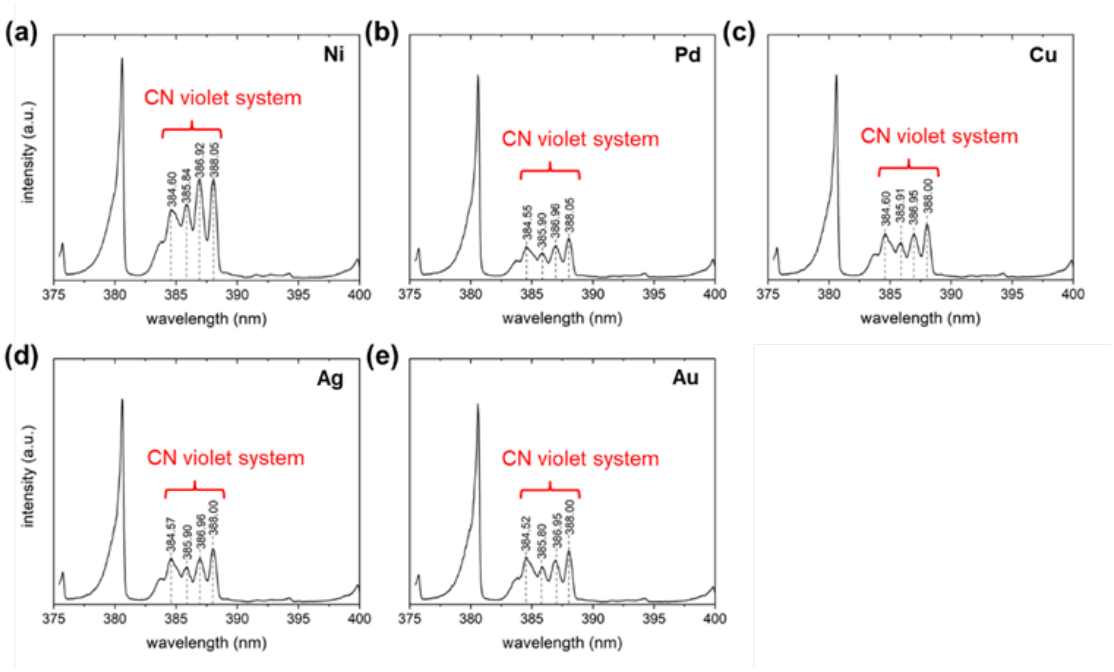

Figure 24. Optical emission spectrum with (a) Ni, (b) Pd, (c) Cu, (d) Ag, and (e) Au surface during the subsequent N_2 exposure in CH_4-N_2 sequential exposure.

In the N_2-CH_4 exposure (Figure 25), when surfaces were first exposed to plasma-activated N_2, adsorption of NCO species on every surface was observed. However, subsequent plasma-activated CH_4 species exposure did not result in the appearance of 1500~1700 cm^{-1} (C=N and C=C) and 2000~2200 cm^{-1} (C≡N and C≡C) features. At the same time, optical emission spectra during subsequent CH_4 exposure with plasma stimulation (Figure 26) only show the presence of CH radical species but not CN radical species. This result indicates that surface-adsorbed NCO does not promote further formation of C-N coupled species.

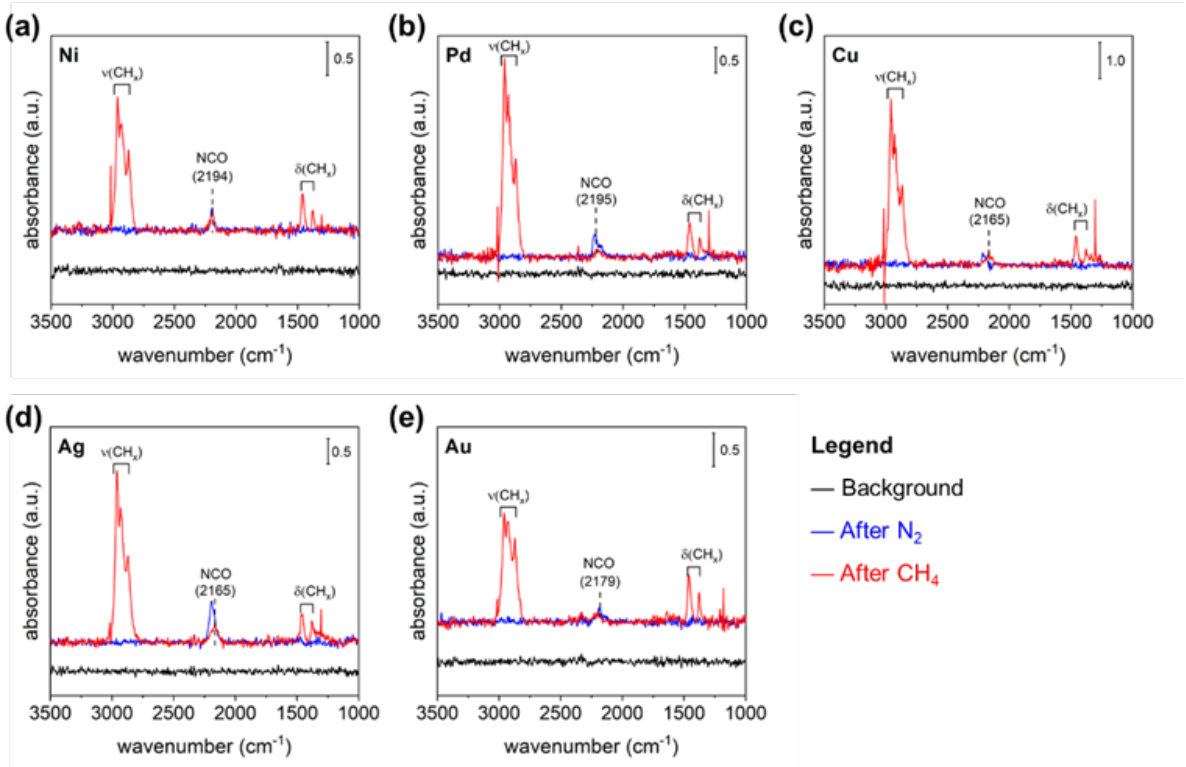

Figure 25. PM-IRAS spectra of adsorbed species on (a) Ni, (b) Pd, (c) Cu, (d) Ag, and (e) Au at 25 °C in sequential N_2-CH_4 exposure (blue: after 30 minutes N_2 exposure & red: after subsequent 30 minutes of CH_4 exposure). Surfaces were treated with an Ar plasma jet at ~20 kHz and 7 kV (peak-to-peak) into either CH_4 or N_2 atmosphere at 1 atm for 30 min.

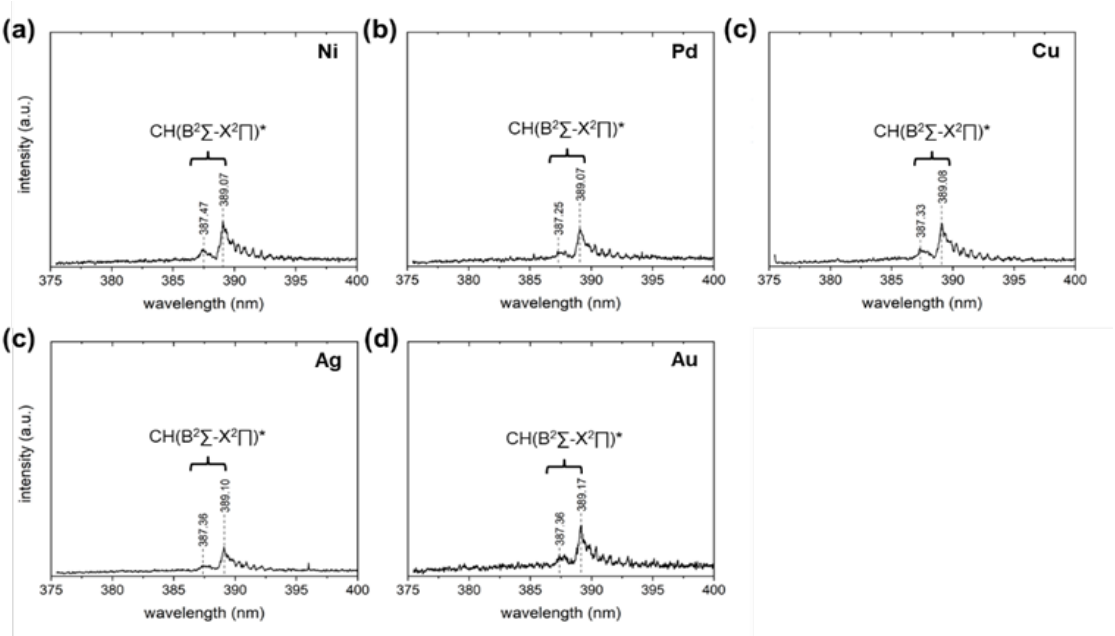

Figure 26. Optical emission spectrum with (a) Ni, (b) Pd, (c) Cu, (d) Ag, and (e) Au surface during the subsequent CH_4 exposure in N_2-CH_4 sequential exposure.

Finally, an equal volume ratio of CH_4 and N_2 was simultaneously introduced to the system with plasma stimulation in the presence of the different metal surfaces (Ni, Pd, Cu, Ag, and Au). Simultaneous exposure also resulted in the appearance of features in 1300~1500 cm^{-1} (CH_x bending), 1500~1700 cm^{-1} (C=N and C=C), 2000~2200 cm^{-1} (C≡N and C≡C), and 2800~3000 cm^{-1} (CH_x stretching) regions during the plasma exposure (Figure 27). During the plasma exposure in 1:1 simultaneous exposure, we observed the presence of strong emission from a CN violet band in the plasma phase (Figure 28). Unlike CH_4-N_2 sequential exposure, PM-IRAS features in 2000~2200 cm^{-1} (C≡N and C≡C) with simultaneous exposure exhibit noticeable differences with Cu and Ag compared to others.

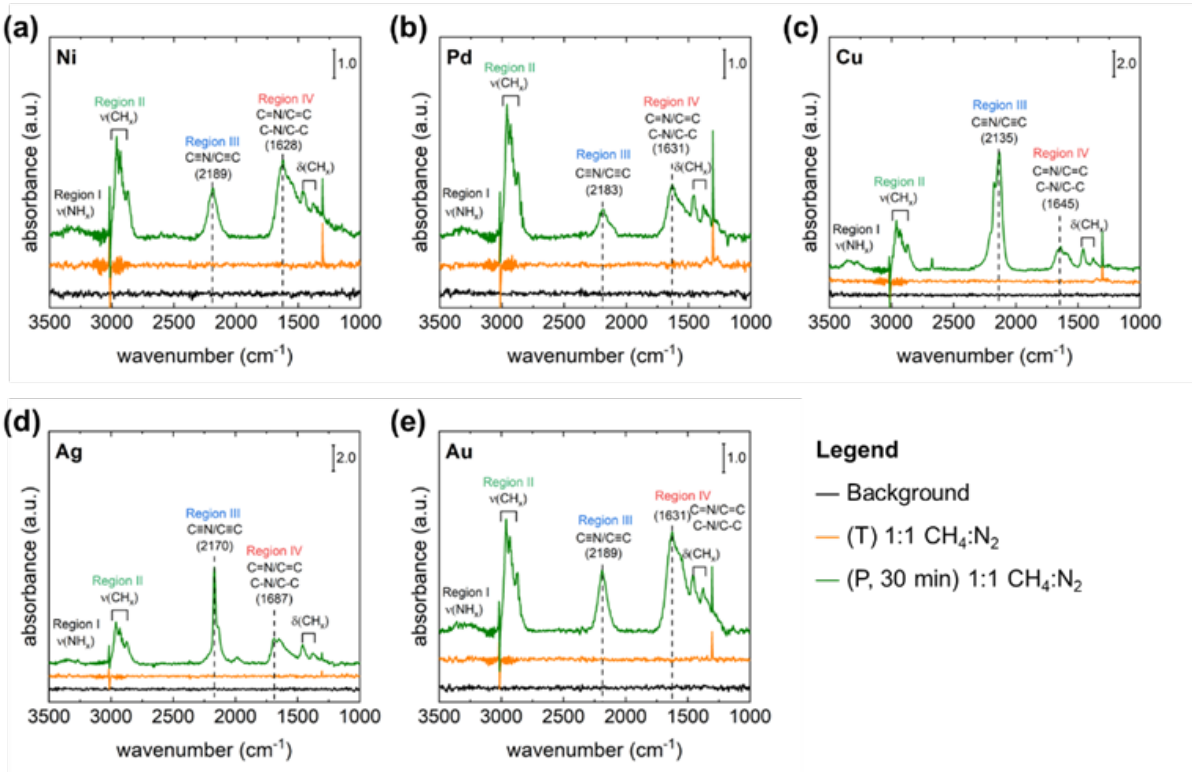

Figure 27. PM-IRAS spectra of adsorbed species on (a) Ni, (b) Pd, (c) Cu, (d) Ag, and (e) Au treated using the following sequence: (black) background thermal Ar exposure at 25 °C, (orange) thermal Ar + 1:1 CH_4:N_2 exposure at 25 °C, and (green) exposure with an Ar plasma jet at ~20 kHz and 7 kV (peak-to-peak) into a Ar + CH_4:N_2 atmosphere at 25 °C for 30 min.

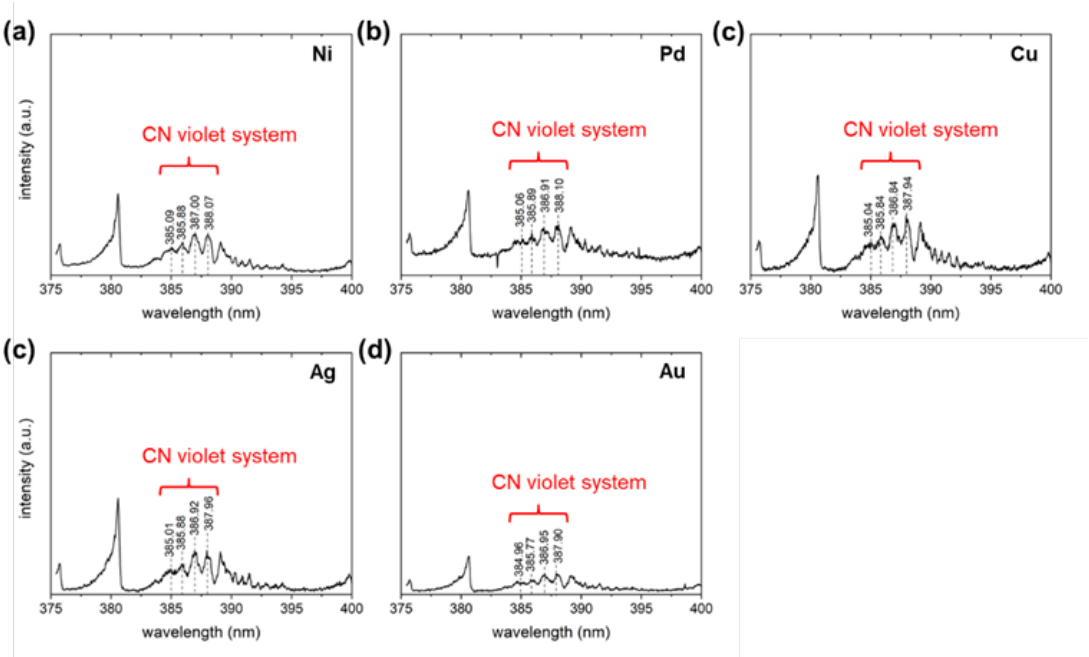

Figure 28. Optical emission spectrum with (a) Ni, (b) Pd, (c) Cu, (d) Ag, and (e) Au surface during 1:1 CH_4:N_2 simultaneous exposure.

Sequential exposure *in-situ* results indicate that surface-adsorbed CHx species and plasma-phase CN radicals may be important intermediate species to form surface C-N coupled species. Simultaneous exposure PM-IRAS results indicate different surfaces can affect the formation of different C-N coupled species.

Plasma Characterization(Subtasks 2.3, 4.1, and 4.2)

In initial experiments, we integrated an optical path with our plasma reactor and investigated the optical emission of various gas feeds, primarily CH_4/N_2 and C_2H_6/N_2 plasma as a function of changing gas composition, plasma power, and bulk gas temperature. We utilized optical emission spectroscopy (OES) to analyze plasma light emission. Initial spectroscopic data was obtained using an Ocean Optics spectrometer, then a Princeton Instruments Fergie. The validation of our OES technique using N_2 was done by measuring the 2nd positive band system (electronic transition) from 320-380 nm. We were able to observe key species in the plasma, but higher resolution imaging was needed in order to better resolve vibrational and rotational lines in the plasma. We eventually settled on collecting optical data using an Andor 500i spectrometer as it was able to provide the best resolution needed for our experiments. Highly resolved images of key species (CH – 431 nm, C_2 – 516 nm, H_β – 486 nm, CN – 388 nm, NH – 336 nm, and N_2 second positive system – 340-380 nm) are shown in Figure 29.

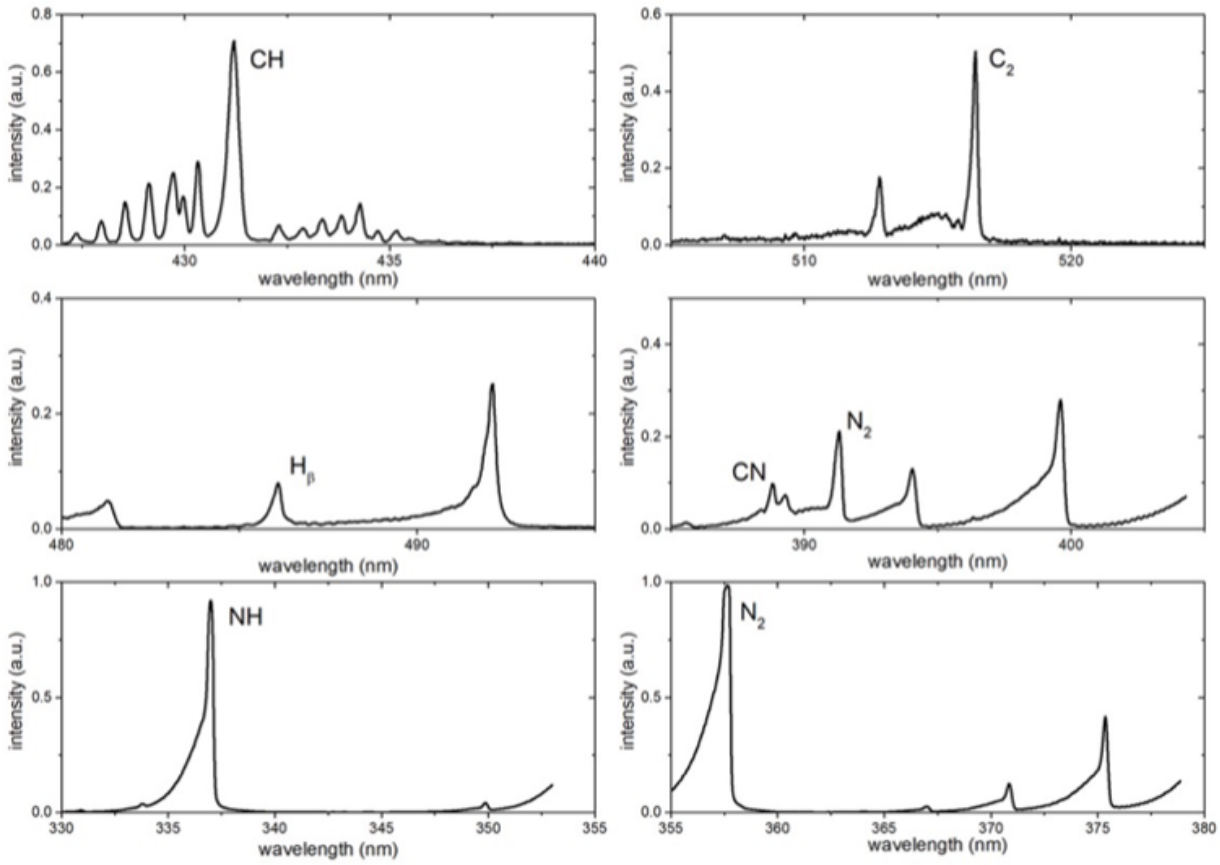

Figure 29. Highly resolved spectra of CH_4/N_2 plasma, showing key plasma species at various wavelengths as indicated in Subtask 4.2, enabling for optical characterization of hydrocarbon-nitrogen coupling.

From the highly resolved spectra, we were able to extract important information about the gas phase plasma such as the rotational and vibrational temperatures of key species that provided insight into the energy partitioning in the plasma and the overall plasma temperature, which we assume to be in equilibrium with the rotational states. These temperatures were obtained by fitting theoretical spectra with our measured spectra using commercially available software SPECAIR© and MassiveOES©.

In some experiments, a tracer gas (He or Ar) was added to the hydrocarbon-nitrogen mixture in order to extract additional plasma properties. Addition of a tracer gas (He) emission lines allowed for the calculation of electron temperature. We used the line ratio method to determine the electron temperature of the plasma. We observed trends in electron temperature and light intensity of specific species with varying operating conditions as shown in Figure 30. Results showed an inverse relationship between the electron temperature and CH_4 conversion but a non-monotonic relationship between the relative CN (388 nm) emission intensity to N_2 (391 nm) and CH_4 content in the plasma.

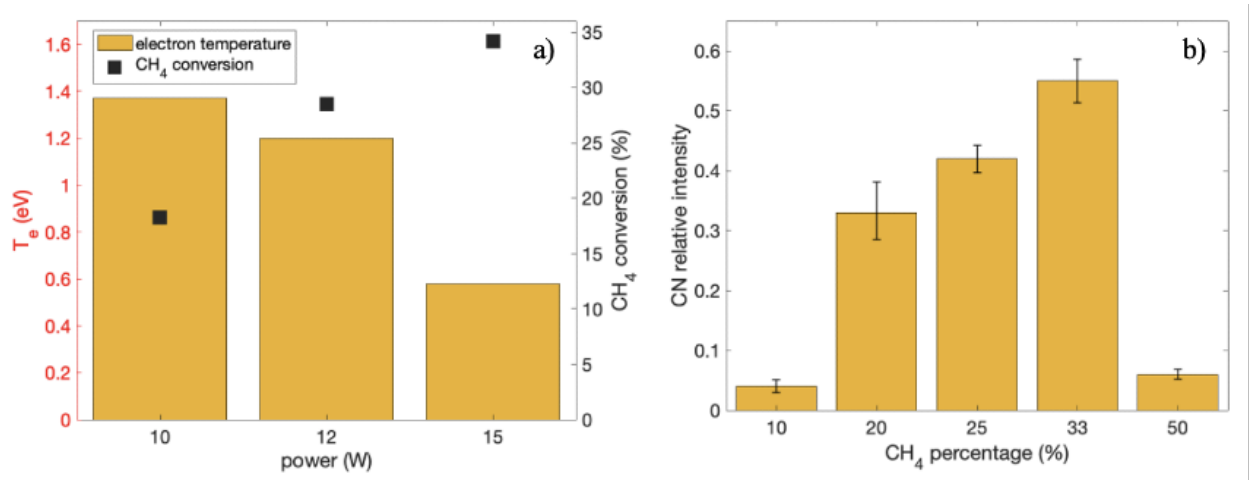

Figure 30. a) Electron temperature and conversion of CH_4 as a function of increasing power showing an inverse relationship between electron temperature and conversion as power increases. b) C-N relative intensity as a function of CH_4 concentration keeping power (10 W), flow rate (50 sccm), and temperature (200 °C) constant.

We were also able to estimate the electron density of the plasma using a Voight profile fitting of the H_β (486 nm) line and relate changes in the electron density to changes in operating conditions as shown in Figure 31. Trends showed a positive correlation between the electron density and CH_4 content, power, and temperature.

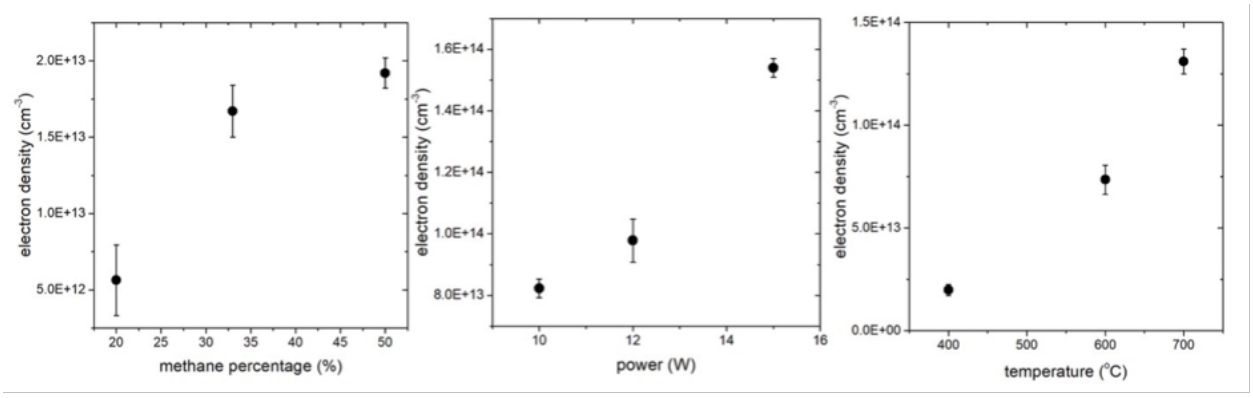

(a) (b) (c)

Figure 31. Electron density is affected by different operating conditions: (a) methane percentage in the gas feed, (b) DBD power, (c) reactor temperature.

In addition to optical characterization, we simultaneously performed electrical characterization of the plasma system. For all plasma reactions, we used electrical characterization of the DBD plasma to quantify the power deposition into the reactor and establish key plasma behavior and properties. We conducted electrical characterization for a variety of gas feeds that corresponded to the optical characterization experiments in both Subtasks 2.3 and 4.2. Current-voltage traces showed the

expected filamentary behavior due to the molecular gases CH_4 and C_2H_6; and at room temperature to about 200 °C, charge-voltage (Lissajous) plots did not show any anomalous behavior.

We mainly focused on pure CH_4/N_2 feeds and maintained the plasma power constant to see how changes in bulk gas temperature affected the plasma characteristics. From the charge-voltage (Lissajous) plots, we have determined that the electrodes become more discharged as temperature increases, which means the plasma expands with increasing temperature as seen in Figure 32.

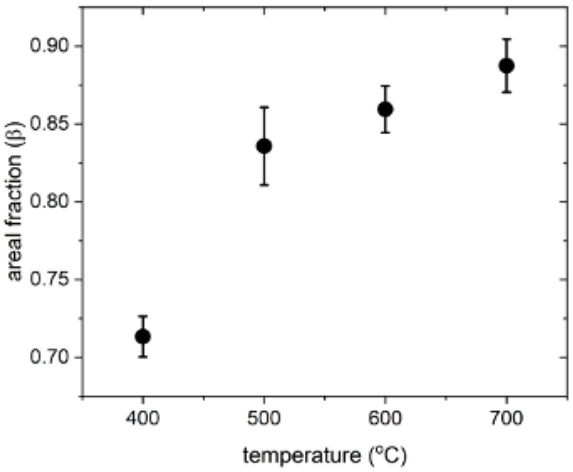

Figure 32. Areal fraction of CH_4/N_2 (1-1) plasma at 50 sccm flow rate and constant power of 10 W at different bulk gas temperatures showing an increase in the discharge area of the plasma.

This was initially attributed to an increase in the permittivity of the dielectric tube as temperature increased, causing changes to the overall resistivity of the system. Analysis from the current-voltage traces showed increase in temperature led to a decrease in the number of filaments while an increase in power has an opposite effect. We also determined some key plasma characteristics such as number of filaments, average current and charge per filament, and the lifetime of a filament in the DBD system. We were able to determine that number of filaments alone was not a good measure of the effects of changing temperature on the system. Rather, average current and charge per filament were better indicators. This was done by creating a surface DBD using different dielectric materials at a constant power and seeing how/whether these characteristics were affected. We were able to determine that an increase in temperature led to a decrease in conversion of CH_4 and the average charge per filament, Q_{avg}, but led to an increase in the discharge cell capacitance and the effective capacitance of the system (Figure 33). We were also able to establish a correlation between changes in certain plasma properties (average charge and lifetime per filament) to methane conversion as shown in Figure 34. This could potentially provide insight into how operating the plasma itself affects the reaction.

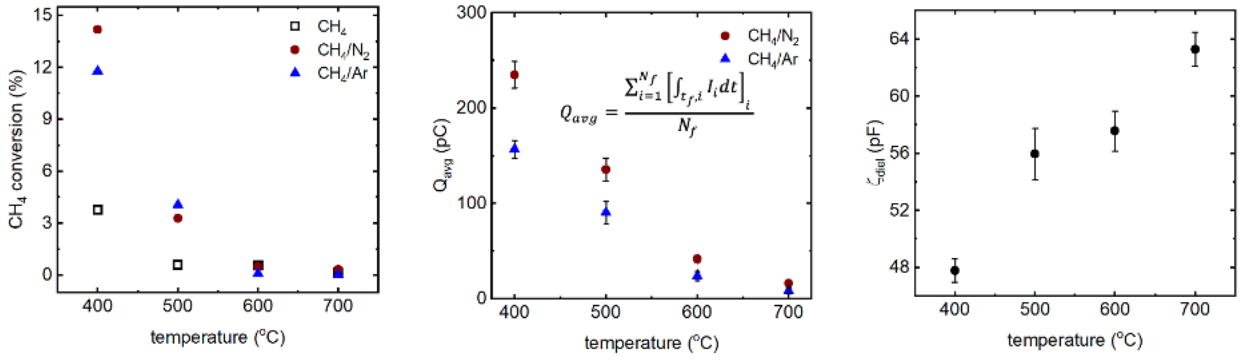

(a) (b) (c)

Figure 33. All gas mixtures were at 50 % CH_4 to N_2/Ar and plasma was at a constant power of 10 W. (a) Conversion of methane reduces with temperature regardless of an additive gas. (b) As temperature increases, there is a reduction in the average charge per filament. (c) An increase in temperature leads to an increase in the effective capacitance of the dielectric which increases the permittivity.

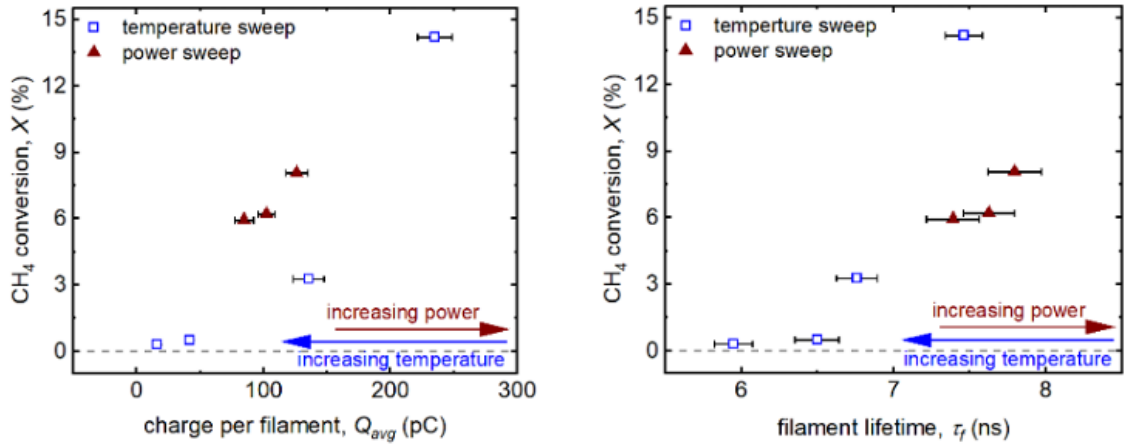

(a) (b)

Figure 34. The initial conversion of methane shows a positive correlation with (a) charge per filament and (b) lifetime per filament in CH_4/N_2 plasmas at various experimental conditions. These relationships can provide insight into how the plasma can directly affect conversion.

While we had initially attributed changes in the measured plasma electrical properties to changes in the permittivity of the quartz tube, analytical predictions of changes in the discharge cell capacitance due to an increase in the dielectric constant of quartz showed there would only be a minimal increase of 0.02 pF, which did not agree with the experimental increase of 8.99 pF. Simulations of electrical circuits at conditions lower than plasma initiation were conducted using LTspice© and it was determined that an increase of in the discharge cell capacitance and changes in the rotation of the Lissajous curve could only be possible due to an increase in the conductivity of the gas with changing temperature. Figure 35 shows how reducing the resistance, and thus increasing the conductivity across the gas from a purely capacitive system with no resistance to 10 MΩ produces an anti-clockwise rotation in the Lissajous curve that agrees with experimental data.

This change in the conductivity of the gas correlates to a decrease in the local gas density but an increase in the electron density, suggesting a pre-ionization occurring in the gas prior to plasma ignition.

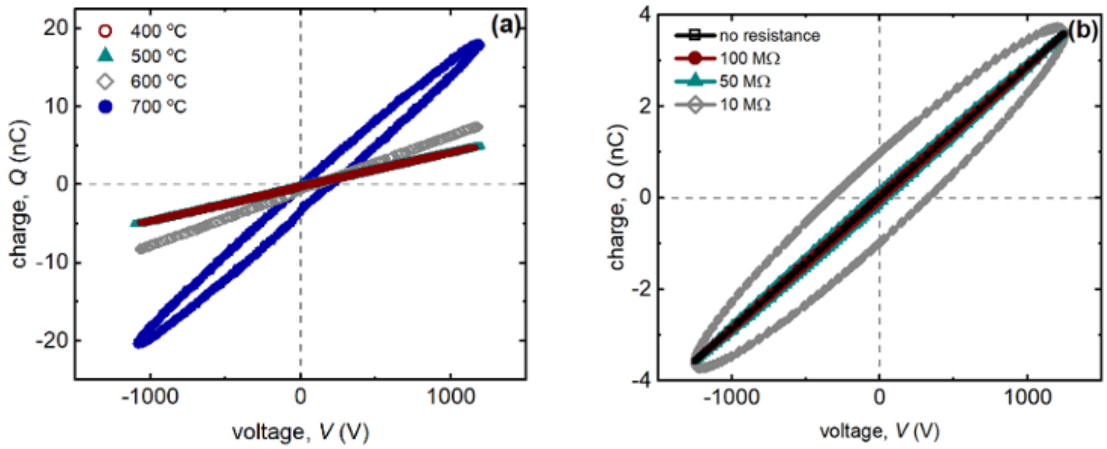

Figure 35. (a) Experimental Lissajous curves below the plasma initiation threshold (applied voltage of 1.25 kV) at varying temperatures. (b) Simulated Lissajous curves with varying resistive elements parallel to the gas capacitance.

Gliding Arc (GA) Plasma Reactor (Subtasks 4.3, 6.2)

We began the process of building a gliding arc reactor as an alternative plasma source as gliding arc plasmas are known to preferentially generate vibrationally excited species relative to DBDs due to their lower reduced electric field. A power supply that could output higher voltages and currents was purchased in order to create and power the arc. We began with a classic design (as opposed to a rotating gliding arc design), with the primary focus being integrated catalyst material as a fluidized bed directly into the effluent of the gliding arc. A schematic of the reactor design is shown in Figure 36.

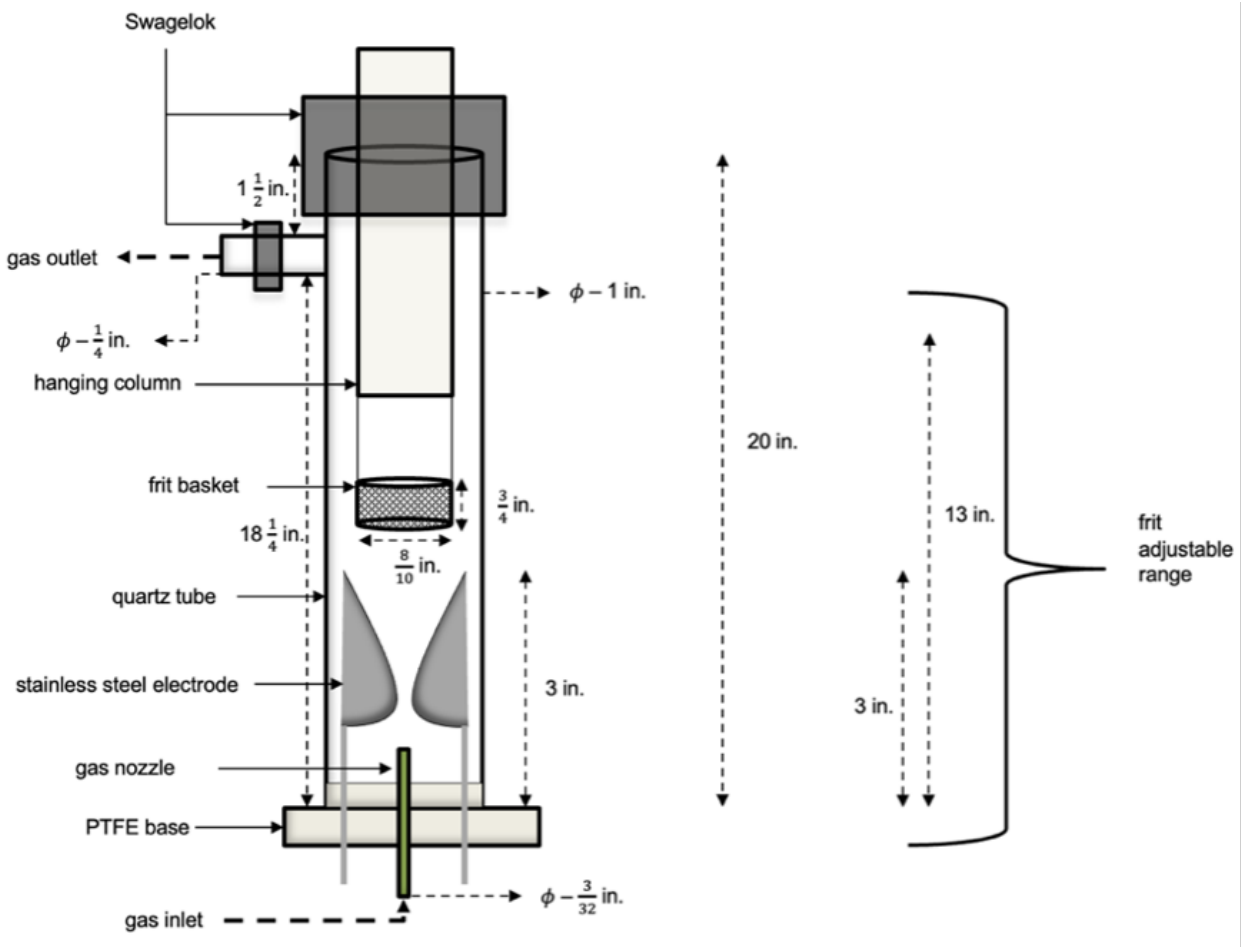

Figure 36. A schematic of the gliding arc reactor which allows for different electrode configurations and a change in the distance between the fluidized catalyst bed and the plasma arc.

Multiple geometries of different electrodes were created to further investigate the propagation of the arc but results were inconclusive. Shorter electrodes did allow for a shorter distance between the gas outlet and the catalyst bed, allowing for fluidization at a lower flow rate. Argon gas was the primary gas used in the arc with an addition of reactive gases to enable easier ignition of the arc. We studied how various resistors in the plasma circuit affected the plasma generation and stability. We observed that a 2.7 kΩ resistor was best at igniting the arc with reasonable applied voltages and currents and creating arcs with average powers upwards of 500 W. An image of an ignited Ar arc and its corresponding electrical traces are shown in Figure 37. We were also able to achieve fluidization and determine that smaller particles (less than 150 μm) were easier to fluidize at flow rates upwards of 9 L min^{-1}.

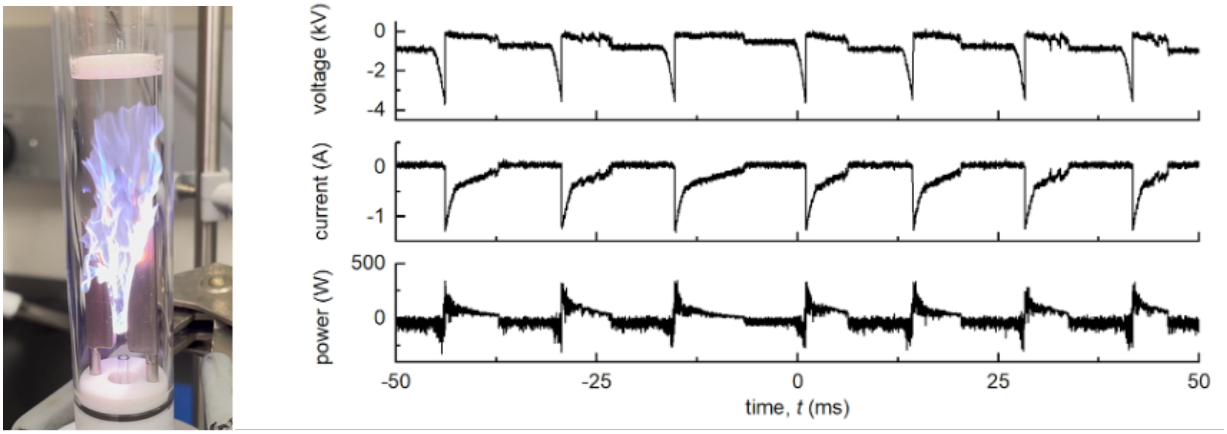

(a) (b)

Figure 37. An image of (a) the Ar gliding arc at 10 L min^{-1} showing high propagation past electrode tips for direct interactions with catalytic bed and (b) measured plasma voltage, current and power of a $CH_4/N_2/Ar$ arc showing strikes corresponding to individual arc formation in the gliding arc. The arc was at a 98 to 1 to 1 argon to nitrogen and methane composition at a flow rate of 10 L min^{-1}, a ballasted 2.7 kΩ resistor, and an applied voltage of -4 kV.

We tested various gas compositions of pure argon as well as Ar and additive mixtures of N_2 and CH_4 up to 20% of the total gas flow within arc stability. Propagation of the arc was drastically affected by the addition of N_2 but not by the addition of CH_4, while ignition of the arc required increased applied voltage and current when other gasses were added to Ar. Optical characterization of the arc using an Ocean Optics spectrometer showed intermediate gas phase species in the plasma as shown in Figure 38 of an Ar/N_2 plasma. Increase in N_2 composition up to 20% of the total feed led to dominant N_2 lines, overshadowing Ar lines in the spectra.

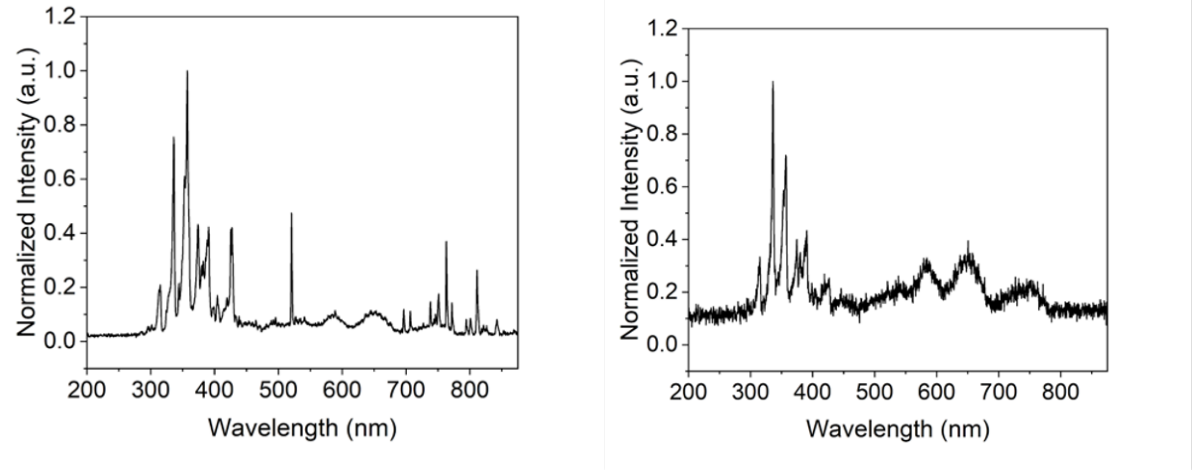

(a) (b)

Figure 38. (a) Normalized Ar/N_2 arc OES spectra at a 95% to 5% composition showing N_2 second positive emission lines as well as Ar lines and (b) normalized Ar/N_2 arc OES spectra at a 80% to 20% composition

showing N_2 second positive emission lines as well as Ar lines. The total flow rate is 10 L min^{-1} with a 2.7 kΩ ballast resistor and an applied voltage of -6 kV.

Keeping a constant applied voltage of 5 kV, current of 175 mA, and flow rate of 9 L min^{-1}, we varied the gas composition of pure Ar and $Ar/CH_4/N_2$ to determine changes to the gas phase products and the electrical properties of the plasma. We tested 4 different gas compositions: (1) Ar/CH_4 (90/10), (2) $Ar/CH_4/N_2$ (90/5/5), (3) $Ar/CH_4/N_2$ (90/9/1), and (4) $Ar/CH_4/N_2$ (90/1/9). Figure 39 shows normalized gas chromatograms at different feed gas compositions. Data were normalized to the highest GC peak (CH_4 peak for all conditions; retention time of ~1 min) and plotted using the same y-axis scale to qualitatively compare the composition of gas-phase products. We observed the formation of heavier hydrocarbons ranging from C2 through C7+ from the reaction.

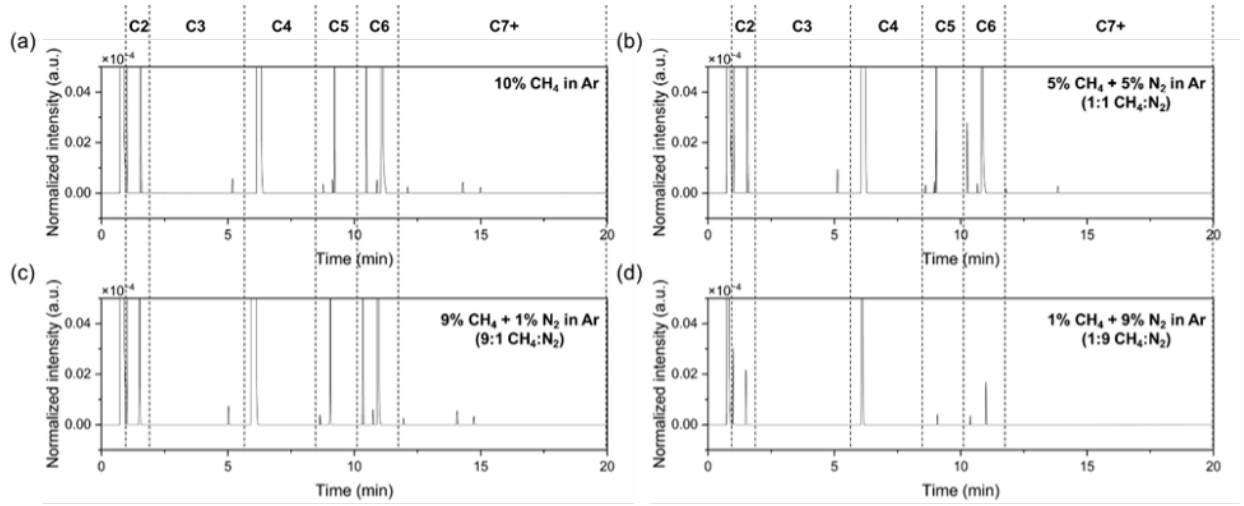

Figure 39. Gas chromatogram of gas phase products formed from CH_4-N_2 reaction at various feed gas compositions using gliding arc reactor system: (a) Ar/CH_4 (90/10), (b) $Ar/CH_4/N_2$ (90/5/5), (C) $Ar/CH_4/N_2$ (90/9/1), and (d) $Ar/CH_4/N_2$ (90/1/9). The total gas flow rate was fixed at 9 L/min. Data were normalized to CH_4 peak (~1 min retention time).

Electrical signals of the arc at 9 L min^{-1} showed that gliding arcs of pure Ar have average arc formation frequencies of 83.4 Hz with average peak powers of 262.0 W. The addition of reactive gases to the Ar arc changed the electrical properties by reducing the arc formation as well as increasing the average peak power of the plasma. In a CH_4 lean (1-9 CH_4 to N_2) environment, the frequency of arc formation reduced from 83.4 Hz in pure Ar to 73.3 Hz and the average peak arc power increases to 501.0 W. In a CH_4-rich (9-1 CH_4 to N_2) environment, the arc frequency further reduced to 70.3 Hz and the arc power increases to 557.9 W. We were able to upscale the reaction to three times the flow with a flow rate of 30 L min^{-1} and observed a higher arc formation frequency of 110 Hz in a pure Ar arc with an average power of 327.5 W at the same applied voltage of 5 kV.

11. NEXT STEPS

For this project to advance to the next TRL, the plasma catalysis N-C coupling technology will need to be assessed in a simulated environment. For this application, the feed gas stream should resemble the composition of shale gas from a production site. The results from the laboratory scale testing could be directly compared with the results from the actual production environment, and the effects on the catalyst lifetime, product selectivity, product yields, and energy efficiency from operation in the realistic environment would be assessed. This technology is still in the early development stages and questions remain. The identification of proper operating conditions and plasma/catalyst configurations to increase product selectivity and reaction efficiency are needed before being subjected to the complexity of the realistic environment.

Heterocyclic aromatic compounds are important in the synthesis of natural compounds, medicinal chemistry, and agrochemicals, and pharmaceuticals. It is expected that these markets will continue to grow in the near future. Deployment of this technology will take advantage of “small-scale”, modular reactor systems, and much can be learned and potentially adapted from deployment strategies for distributed ammonia synthesis, distributed methanol synthesis, and non-thermal plasma ozone generation concepts.

12. PRODUCTS

1. Bogaerts, A.; Tu, X.; Whitehead, J.C.; Centi, G.; Lefferts, L.; Guaitella, O.; Azzolina-Jury, F.; Kim, H.-H.; Murphy, A.B.; Schneider, W.F.; Nozaki, T.; Hicks, J.C.; Rousseau, A.; Thevenet, F.; Khacef, A.; Carreon, M.; "The Plasma Catalysis Roadmap", Journal of Physics D: Applied Physics, **2020**, 53, 44, 443001
2. Lee, G., Go, D.B., and O'Brien, C.P ACS Appl. Mater. Interfaces **2021**, 13, 47, 56242–56253.
3. Yan, C.; Waitt, C.; Akintola, I.;Lee, G.; Easa, J.;Clarke, R.; Geng, F.; Poirier, D.; Otor, H.O.; Rivera-Castro, G.; Go, D.B.; O'Brien, C.P.; Hicks, J.C.; Schneider, W.F.; and Ma, H., Industrial & Engineering Chemistry Research **2022** 61 (23), 7675-7678, DOI: 10.1021/acs.iecr.2c01594
4. Akintola, I.; Rivera-Castro, G.; Yang, J.; Secrist, J.; Hicks, J. C.; Veloso, F.; and Go, D.B., Plasma Chemistry and Plasma Processing, **2023**, 43, 6, 1999-2016. DOI: 10.1007/s11090-023-10388-x
5. Rivera-Castro, G.; Scotto d'Apollonia, A.; Cho, Y.; and Hicks, J.C., Industrial & Engineering Chemistry Research **2023** 62 (44), 18394-18402, DOI: 10.1021/acs.iecr.3c02812
6. Clarke, R.; and Hicks, J.C., The Journal of Physical Chemistry C **2023** 127 (31), 15239-15245, DOI: 10.1021/acs.jpcc.3c03268
7. Poirier, D.; Hale, D.; Barboun, P.M.; and Hicks, J.C., Journal of Environmental Chemical Engineering, **2024**, 12, 2, 111970. https://doi.org/10.1016/j.jece.2024.111970.
8. Lee, G.; Yan, C.; Schneider, W.F.; Go, D.B.; and O'Brien, C.P., ACS Applied Materials & Interfaces **2024** 16 (4), 4561-4569, DOI: 10.1021/acsami.3c14965
9. Hicks, J.C.; Poirier, D.; Rivera-Castro, G.; Systems and methods for processing shale gas, **2024**, 18/345,866.
10. Hicks, J.C.; Rivera-Castro, G.; Systems and methods for processing gas streams, **2024**, 18/345,908.
11. Lee, G., Go, D.B., and O'Brien, C.P; submitted – under review.

APPENDIX: Final Technoeconomic Evaluation

EXECUTIVE SUMMARY

This final technoeconomic report details the synthesis of N-containing liquids and other longer chain hydrocarbon products from plasma stimulation of CH_4 and N_2 feeds. Flaring light hydrocarbons from wells and refineries amounts to a global, annual loss of >140 billion m^3 of natural gas.[1] Not only are valuable, non-renewable hydrocarbons misused during this process, but flaring also contributes more than 400 metric tons of CO_2 to the environment.[1] The implementation of chemical processing technology that directly converts light gases to liquid products will relieve the strain associated with gas separations and gas compression at the source.

We provide an Aspen Pro simulation for N_2 activation and C-H activation together in a plasma-assisted, catalytic reaction system to produce high-value chemicals at near-ambient conditions. The reaction network was modeled as seven consecutive reactions starting with CH_4 and N_2 to generate pyrrole (a model compound representing the N-containing liquid products). We simulated the reaction system to pyrrole because it is observed as a product (in minor quantities), but it was also another N-containing liquid species beyond HCN that we could include in the Aspen Pro simulation. The assumption here is that pyrrole represents the entire liquid stream, which can contain a variety of N-containing products (see Appendix). Additionally, two different feed ratios (CH_4/N_2 = 1 and 1/3) were considered in the process by keeping the inlet flow of CH_4 at 50,000 scf/day. The purpose of this analysis was to understand the sensitivity of the process to the capital and operating costs associated with the more dilute and larger volume CH_4/N_2 = 1/3 system.

The benefits of the Notre Dame (ND) process include the production of highly valuable products, production of liquid-phase products (ease of transportation from well-head), and potentially a lower energy consumption to activate CH_4 and N_2 compared to thermal approaches. The profitability of the entire plant was examined and determined to be strongly influenced by the product distribution and product selling price. If the liquid product stream was assumed as only pyrrole selling at a 99% discounted price, the annual revenue would be ~$890,000; however, it would not be profitable over the plant life. This was expected and was not representative of the actual product distribution. Therefore, we averaged the price of the product stream based on experimental data. With this assumption and a 99% discounted price for the liquid product stream, the annual revenue exceeded $84 million/well with a discounted cash flow rate of return >900% and a payback period of less than a year. Depending on the product, a conservative estimate of the market size is >$500 million, such that it can be concluded that the technology has significant commercialization potential.

1. INTRODUCTION

This report contains a Final Technoeconomic Evaluation (TEA) for project DE-FE0031862, "Process Intensification by One-Step, Plasma-Assisted Catalytic Synthesis of Liquid Chemicals from Light Hydrocarbons". The TEA is directly responsive to the requirements in the Department of Energy (DOE), Office of Fossil Energy (FE), Advanced Natural Gas Infrastructure Technology Development Funding Opportunity Announcement (FOA) DE-FOA-0002006.

The U.S. Energy Information Administration (EIA) is estimating that natural gas production from shale resources will increase for decades.[2] Currently, the majority of natural gas is used as a fuel source, with minor portions being used to create chemicals, fertilizers, and hydrogen gas.[1] Due to the abundance of natural gas (primarily methane with smaller fractions of C_2-C_4), there is an opportunity to use more of the natural gas for purposes aside from energy production. One particular use, creating nitrogen-containing compounds, is important because these compounds are precursors in the synthesis of antibiotics, fungicides, anti-inflammatory medications, medications for reducing cholesterol, etc.

Although conversion of natural gas into nitrogen containing compounds (e.g., hydrogen cyanide, HCN) can be realized using thermal and catalytic approaches, these routes often require ammonia as the N-source[3, 4] resulting in complicated synthesis pathways from N_2, low HCN yields (Andrussow process)[5], and/or energy intensive methods (>1500 K; Degussa BMA process).[5] The objective of this project is to develop a modular and flexible plasma-assisted, catalytic process to convert light hydrocarbons (e.g., methane, ethane) and molecular nitrogen (N_2) into liquid chemicals that contain C-N bonds. From our ongoing experimental efforts, liquid N-containing hydrocarbons are observed from plasma stimulation of N_2-rich hydrocarbon streams (e.g., methane and ethane). For both methane and ethane feeds, an increase in hydrocarbon product yield is observed when the input power is increased. As the N_2 partial pressure is increased in the feed, an increase in the N-containing products is also observed. We are currently in the process of identifying and quantifying the multiple gas phase products and >30 liquid phase products from these catalyst-free experiments (see Table A1 for some of the identified liquid products). Overall, we see that the specific energy input from the plasma drives the hydrocarbon conversion, and the gas phase composition drives the product distribution and composition.

This final TEA provides an overview of the technology pursued in this project, the process model and assumptions, capital and operating cost considerations, results and discussion of the findings, and concluding remarks with plans for updating the model during the duration of the award. As noted by NETL,[6] the purpose of a TEA is to provide guidance to the research program and to monitor the progress of the proposed technology as it relates to meeting the goals set by DOE. This initial TEA will be updated throughout the duration of the project and provide guidance for advancement through the various technology readiness levels (TRLs).

2. TECHNOLOGY RISKS AND MARKET ASSESSMENT

As noted above, our research team has identified an opportunity to utilize a modular reactor that inputs natural gas from the natural gas-producing well-head and nitrogen from atmospheric air to produce nitrogen-containing compounds through a plasma-stimulated reaction process. Currently, oil and gas companies constantly evaluate whether to capture and sell the gas based on current prices or to flare the gas. Further, it is often common to flare the gas at well-heads that are isolated (or stranded) and do not have proper piping infrastructure.

Through collaboration with the Innovation, De-Risking and Enterprise Acceleration (IDEA) Center at the University of Notre Dame, a team of analysts[7] considered the technological risks associated with this project, including a market assessment. Every early-stage technology will have many risks associated with commercialization. In order to effectively commercialize a technology, the number and severity of these risks must be significantly reduced. To address these liabilities, the ND Commercialization Engine has been designed around a term called "de-risking". De-risking is a systemized process whereby the many liabilities associated with early-stage technologies are increasingly mitigated and/or neutralized. This, in turn, gradually transforms the technologies into nascent products ready to be licensed to an outside entity. The de-risking process begins with a comprehensive risk assessment strategy, and this assessment is regularly updated throughout the process. In this section, we highlight the major findings from the internal assessment.[7]

Figure A1 shows the process technology scorecard from the internal technology risk assessment. The assessment considered customer validation, competitor risk, market size risk, technology risk, technology development risk, protectability risks, and regulatory barriers with various categories for each of the risks. The major findings include the following:

- *Customer Validation*: Identified hypothetical beachhead market. Oil companies with well-heads that produce primarily oil and do not have gas piping infrastructure typically flare gas because gas production is not profitable. If given a way to profit off of a resource they are currently burning and releasing into the atmosphere, they would most likely take the opportunity.
- *Competitor Risks:* Competitors basically satisfy customers. Oil companies currently make the majority of their revenue at a well-head from oil production. Gas production is an added benefit if market conditions permit a profitable sale. If gas prices are low enough that it is not profitable to pursue gas production, oil companies can flare the gas at essentially no extra cost, and regulations are not yet in place to reduce greenhouse gas emissions from flaring.
- *Market Size Risk:* The total available market (TAM) from the assessment is > $500 million.
- *Protectability Risk:* This risk is relatively low. The research team has a clear space and is likely to achieve broad claims, trade secrets, or first to market.

- *Regulatory Barriers:* No regulatory barriers found. Any regulation would be done by chemical companies that purchase the products.

The comparison of this technology to current methods to utilize natural gas is found in Figure 1. The three main competitors for natural gas usage are either not lucrative enough or require large central processing plants. The benefits of the ND process include the production of highly valuable products (N-containing hydrocarbons are valuable -- see Table A1), production of liquid-phase products (ease of transportation from well-head), and potentially a lower energy consumption to activate CH_4 and N_2 compared to thermal approaches. The potential negatives of the process include the production of reactive/hazardous products and the reaction selectivity. Research is ongoing to develop process conditions and/or identify catalytic materials to control the product distribution.

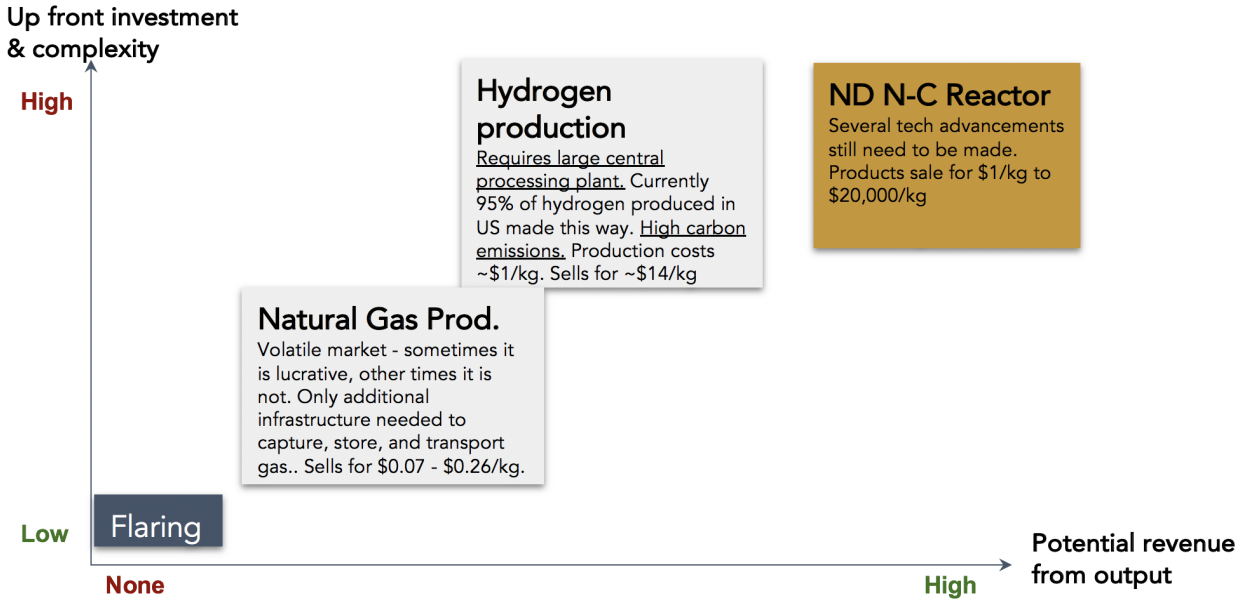

Figure 1. Upfront investment and process complexity vs. potential revenue for various uses of natural gas resources.

The triazole components have direct application as pharmaceuticals and fungicides. The global fungicide market was estimated at $18.7 billion in 2019 with a projected growth to $24.5 billion by 2025.[8] Similarly, the global pyrrole market size was $6.2 million in 2019. Therefore, depending on the product, a conservative estimate of the market size is >$500 million, and the technology has significant potential as a startup candidate.

3. PROCESS MODEL AND ASSUMPTIONS

The conversion of light hydrocarbons and molecular nitrogen into longer chain hydrocarbons containing N-C bonds in the presence of plasma stimulation is a new discovery by our research team. Therefore, the reaction network is largely unknown and likely occurs through a variety of

radical reactions induced by the plasma. Aspen Plus process simulator was used to model this process using experimental data from lab-scale reactor operation as the basis. Aspen Plus is a process simulation package commonly used in industry to evaluate the performance of a process based on the various unit operations and the thermodynamic models selected by the user.

A general block flow diagram of the ND process is shown in Figure 2. The two feeds are methane and N_2. For the purpose of this technoeconomic evaluation, the methane feed is considered pure and at 50,000 scf/day. The N_2 feed is assumed to be from an on-site N_2 enrichment unit and fed at a 1:1 or 1:3 methane to N_2 volumetric flow rate ratio. The reactor converts the feed into a variety of gases and liquids, which are separated in a flash drum downstream.

The reactor is modeled using a RSTOIC reactor in Aspen Plus. This reactor allows for multiple reactions to be included in which the user inputs the reaction conversion for each reaction. Because this technology is in the early stages of development, specific information regarding the reaction network, carbon balance, and all possible produced products is currently unknown and part of the ongoing experimental portion of the project. However, we are able to determine the conversion of the hydrocarbon feed, and in the process, identify and quantify the gas phase products. For this initial technoeconomic analysis, the reaction network modeled in Aspen Pro is shown in Table 1. For the simulation, the reactions are considered to occur consecutively, starting with the initial homologation of methane to ethane and hydrogen in Reaction 1. The initial N-C coupling reaction occurs in Reaction 2, where methane and nitrogen react to form ammonia (NH_3) and hydrogen cyanide (HCN). The series of reactions were selected to provide a pathway to produce N-containing liquids. Although we observe > 30 liquid products in some of the experiments, we selected pyrrole as the product because it is observed as a product in many cases and has a selling price that is lower compared to other N-containing products observed (Table S1).

A)

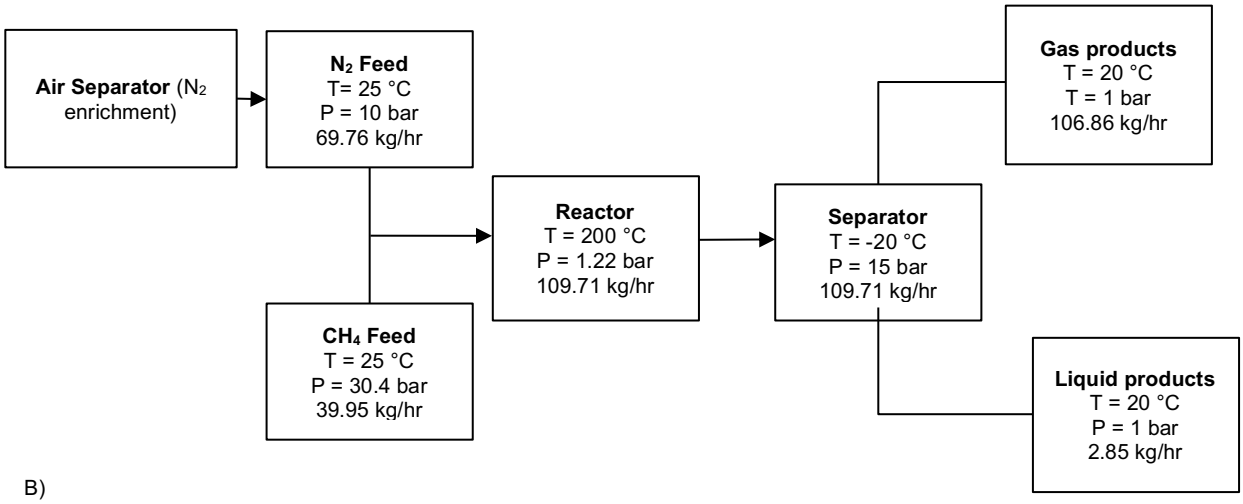

B)

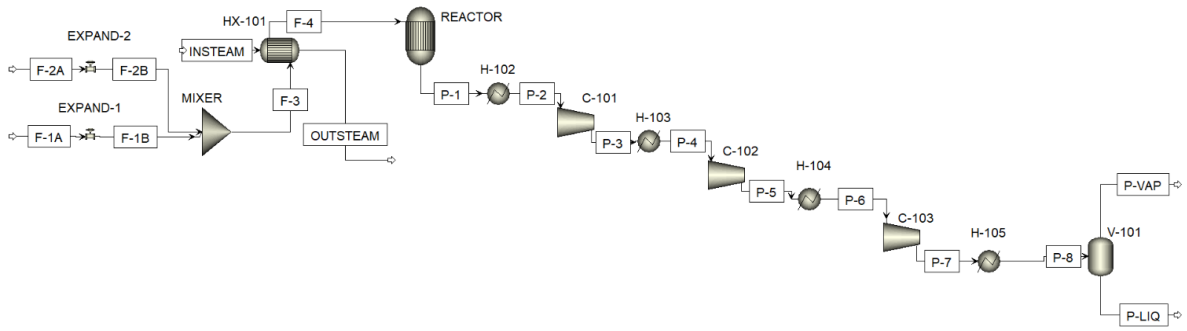

Figure 2. A) Block flow diagram for the ND plasma-assisted N-C coupling process, and B) Aspen Pro flow diagram with units and streams labels.

Table 1. Reactions, reaction enthalpies, and fractional conversions considered in the Aspen Pro simulation.

Reaction #	Reaction	$\Delta H^{o}_{Reaction}$ (kJ/mol)	Fractional Conversion (limiting reagent)
1	$2CH_4 \rightarrow C_2H_6 + H_2$	65.2	0.087 (CH_4)
2	$CH_4 + N_2 \rightarrow NH_3 + HCN$	160.7	0.02 (CH_4)
3	$C_2H_6 \rightarrow C_2H_4 + H_2$	136.4	0.015 (C_2H_6)
4	$CH_4 + C_2H_6 \rightarrow C_3H_8 + H_2$	53.9	0.043 (CH_4)
5	$C_3H_8 \rightarrow C_3H_6 + H_2$	124.4	0.992 (C_3H_8)
6	$C_3H_6 \rightarrow C_3H_4 + H_2$	165.7	0.997 (C_3H_6)
7	$C_3H_4 + HCN \rightarrow C_4H_5N$	-209.2	1.0 (HCN)

The major assumptions in this model are provided below:

- Natural gas is primarily composed of methane, ethane, and CO_2. Trace amounts of N_2, H_2O and H_2S are also present in some wells. However, the actual composition of the gas varies from region-to-region and well-to-well. In most cases, the majority of the gas is methane. Therefore, the shale gas feed in the simulation is assumed to be methane for simplification purposes.[9]
- The Peng-Robinson equation of state, which is commonly used with hydrocarbon mixtures, was chosen as the thermodynamic property method. This method is suitable for analyzing natural gas at a well-head, and it was used for calculating phase equilibrium.[10]
- All heat exchangers were modeled as countercurrent heat exchangers with a minimum temperature approach of 10 ^oC. Heat transfer coefficients were estimated based on the characteristics of the exchanger.
- The maximum outlet temperature of the compressed gas stream was chosen as 175 ^oC.[11] The ratio for each compression was calculated as $(P_n/P_1)^{1/n}$ where n is the number of the compressor in the staged compression sequence. The ratio was kept constant for each compressor.[12]
- The flash was modeled as a combination of a heat exchanger to lower the temperature of the stream and a flash drum to decrease the pressure and separate the stream into two phases. The length to diameter ratio was estimated as 4, which fits the optimum ratio range (2.5 to 5). The required holdup time for gas/liquid separation was estimated at 5 minutes.[12]
- No hydrogen cyanide (HCN) is included in the byproduct and complete fractional conversion for this species is assumed in the reactor design.
- The plasma reactor design for this project was adapted from the design of commercial plasma ozone generators.[13] Specifically, 174 cylindrical discharge tubes of about 50 mm diameter and 3 m length are installed as a bundle of tubes which constitutes the plasma reactor. Pyrex (Duran) glass tubes are mounted inside slightly wider stainless steel tubes to form annular discharge gaps of about 1 mm radial width.[13] The inner layer of glass tubes is coated with thin aluminum, serving as a high voltage electrode and the outer layer of stainless steel tubes are designed to be ground electrodes.[13] Therefore the plasma discharge zone has the length of 3 m, with a discharge volume of 226 ml/each tube. Based on this discharge volume and our current residence time of 0.02 s in our lab-scale reactor, we estimate the flow rate for each tube to be ~11,304 ml/min. The total number of tubes in the reactor is 174 in order to satisfy the total flow rate (100,000 scf/day). All of these tubes are installed in a large steel tank in the same configuration as a tube-shell heat exchanger. Gas feed flows through the tube and heating from natural gas can pass through the inner space between the plasma tubes to provide heat exchange and an isothermal environment.
- The cost of the plasma reactor was estimated based on the six-tenth factor where $Cost_1/Cost_2 = (size_1/size_2)^{0.6}$.[14] One lab-scale plasma reactor was estimated to cost ~ $8000.
- One spare reactor (174 tubes per reactor) is needed for the plant so that it can be operational when the primary reactor is under maintenance or when operated to remove residual carbon

from the reaction. As the project matures, we may identify the need for more reactors to cycle between while the residual carbon is removed from fouled reactors.

- The gas feed is methane from natural gas and nitrogen generated from an air separation. Their costs are estimated based on the price of shale gas and separation cost of nitrogen through a commercial membrane available on-site. A quote for a membrane was obtained from Generon (Model 6800CP) for $18,404 with operating conditions of 99.5% N_2 purity at 6.9 barg and 805.2 SCFH.
- No land costs were included in this model since this is designed to operate as a mobile system.
- CAPCOST was utilized to calculate the cost of equipment/manufacturing and for the generation of the cash flow diagrams.

The simulation was conducted at two different CH_4/N_2 ratios (= 1 and = 1/3) due to the increased N-containing liquids observed experimentally under N_2 rich conditions. The stream table for the 1:1 feed is shown in Tables 2 and 3. The high pressure methane and nitrogen was passed through expansion valves to lower their pressure before being mixed. The mixed feed was heated to 200 ^oC using high pressure steam and fed to the reactor which operates at 200 ^oC and 1.2 bar. Based on experimental results, the overall methane conversion was set to 15 %, and the mass fraction of ethane and propane in the product stream were set to 0.003 and 0.0003, respectively. The reactions produced a variety of gas phase products, and a staged compression was used to pressurize the stream before flashing it to separate out liquid pyrrole. Approximately 2.84 kg/hr of pyrrole was collected in the liquid product stream, which had a mass composition of 0.996 pyrrole.

A similar analysis was performed for $CH_4/N_2 = 1/3$, where the amount of nitrogen fed to the reactor was tripled. The steam tables for the $CH_4/N_2 = 1/3$ are located in Table A2 and A3. To represent experimental conditions, the methane conversion in the reactor was set to 18%, and the mass fraction of ethane in the product stream was 0.0016. After compressing and flashing the products, 4.09 kg/hr of pyrrole was collected in the liquid stream with a mass composition of 0.998 pyrrole.

Table 2. Stream table for feed streams through the reactor in the simulated ND process for CH_4/N_2 = 1.

	F-1A	F-2A	F-1B	F-2B	F-3	F-4	P-1	P-2
Temperature (°C)	25	25	10.5	22.95	16.1	200	200	35
Pressure (bar)	30.4	10.0	2.0	2.0	2.0	2.0	1.2	1.2
Flows (kg/hr)								
Methane	39.95	0.0	39.95	0.0	39.95	39.95	34.2	34.2
Nitrogen	0.0	69.8	0.0	69.8	69.8	69.8	68.5	68.5
Ethane	0.0	0.0	0.0	0.0	0.0	0.0	0.33	0.33
Ethylene	0.0	0.0	0.0	0.0	0.0	0.0	0.05	0.05
Ammonia	0.0	0.0	0.0	0.0	0.0	0.0	0.77	0.77
Hydrogen	0.0	0.0	0.0	0.0	0.0	0.0	0.80	0.80
Propane	0.0	0.0	0.0	0.0	0.0	0.0	0.03	0.03
Propylene	0.0	0.0	0.0	0.0	0.0	0.0	0.01	0.01
Methyl Acetylene	0.0	0.0	0.0	0.0	0.0	0.0	1.97	1.97
Pyrrole	0.0	0.0	0.0	0.0	0.0	0.0	3.05	3.05

Table 3. Stream table for streams entering the staged compression sequence through the end of the system in the simulated ND process.

	P-3	P-4	P-5	P-6	P-7	P-8	P-VAP	P-LIQ
Temperature (°C)	171	40	148	58	112.4	-20	20	20
Pressure (bar)	3.8	3.8	9.5	9.5	15	15	1	1
Flows (kg/hr)								
Methane	34.2	34.2	34.2	34.2	34.2	34.2	34.2	4.7×10^{-4}
Nitrogen	68.5	68.5	68.5	68.5	68.5	68.5	68.5	1.4×10^{-4}
Ethane	0.33	0.33	0.33	0.33	0.33	0.33	0.33	5.7×10^{-5}
Ethylene	0.05	0.05	0.05	0.05	0.05	0.05	0.05	4.9×10^{-6}
Ammonia	0.77	0.77	0.77	0.77	0.77	0.77	0.77	0.0034
Hydrogen	0.80	0.80	0.80	0.80	0.80	0.80	0.80	3.7×10^{-7}
Propane	0.03	0.03	0.03	0.03	0.03	0.03	0.03	2.3×10^{-5}
Propylene	0.01	0.01	0.01	0.01	0.01	0.01	0.01	8.8×10^{-6}
Methyl Acetylene	1.97	1.97	1.97	1.97	1.97	1.97	1.97	0.008
Pyrrole	3.05	3.05	3.05	3.05	3.05	3.05	0.21	2.8

4. CAPITAL AND OPERATING COST ASSESSMENT

We provide the capital costs associated with building a production system operating at 50,000 scf/day of CH_4. Table 4 provides estimated costs for each unit operation in the process utilizing CAPCOST software. This software allows the calculation of equipment, manufacturing, and total plant cost for a given process. The compressors (C-101, C-102, C-103) are rotary type, and the total cost is based on the horsepower required to compress a given stream. The shell and tube exchangers (E-101, E-102, E-103, E-104, E-105, E-106) are made from stainless steel, and the total cost was estimated using the heat exchange area and operating pressures for both shell and tube sides in the design. E-101 is a shell and tube exchanger which heats the feed gas before feeding it to the reactor. The remaining heat exchangers constitute an interstage cooling process, where low-temperature refrigerated water/refrigerant is used for this purpose (Table 5). The flash drum (V-101) was designed as a stainless steel vessel, and the estimated cost is based on the height

and diameter of the drum. Shown in Table 4, the resulting total capital cost of the process (CH_4/N_2 = 1) was estimated at $806,000 ($824,152 with air separator). This includes two reactors, one of which is a spare reactor that can be used when the other is being cleaned.

Capital and operational costs were estimated following the same procedure for a CH_4/N_2 = 1/3 process. After appropriate sizing of the equipment, estimated costs for each unit operation are estimated at ~$950,000 due to the larger volume of gas that is processed in the system (Table A4). Operational costs for each utility are estimated in the same manner and can be found in Table A5.

Table 4. Total equipment cost for the CH_4/N_2 = 1 process

Equipment Name	Equipment ID	Purchase Cost ($)
Compressor	C-101	34,900
Compressor	C-102	34,900
Compressor	C-103	34,900
Heat Exchanger – 1	E-101	65,800
Heat Exchanger – 2	E-102	57,100
Heat Exchanger – 3	E-103	57,100
Heat Exchanger – 4	E-104	57,600
Heat Exchanger – 5	E-105	58,100
Flash Drum	V-101	8,320
Plasma Reactor (x2)	Z-101/Z-102	353,548
Total Equipment Cost		**$ 805,748 ($824,152 with air separator)**

Table 5. Total annual utility cost for CH_4:N_2 = 1 process

Utility	Annual Utility Cost ($)
Low temperature refrigerated water (5°C)	2,745
Electricity	53,927
Natural gas for heating reactor	6,362
Low temperature refrigerant (-50°C)	2,965
Total Annual Utility Cost	**$68,900**

The operational cost of this economic evaluation is based on four categories: 1) raw material cost (C_{RM}), 2) utility cost (C_{UT}), 3) cost of working labor (C_{OL}), and 4) cost of waste treatment (C_{WT}). As is seen in Table 6, raw material and waste treatment represent a minor portion of the operational cost, while the utility and working labor are major costs. Waste treatment is assumed to be negligible since all the products are sold and cooling water is recycled. Because electricity is used to power the plasma reactors, electricity consumption results in 78% of total utility cost, and it is highly sensitive to the electricity price. Our current estimation is based on the averaged industrial electricity price in 2020 over the US ($6.48/kWh). However, we do acknowledge that the location of the sites may result in significant price variations for the needed electricity. Further, it could be envisioned that renewable sources are used for the electricity (e.g., solar, wind, etc.) which would also increase the price while decreasing the CO_2 footprint. The working labor cost is based on 12 major pieces of equipment in our process and a salary of $28.64/hr. We estimate 14 operators are needed to satisfy the total number of shifts in the operation.

Table 6. Operational cost of the CH_4:N_2 = 1 process

Category	Annual Cost ($)
Raw material (C_{RM})	87,111
Utility (C_{UT})	68,900
Working labor (C_{OL})	834,120
Waste treatment (C_{WT})	negligible

5. PROFITABILITY ANALYSIS

The cost of manufacture without depreciation (COM_d) is calculated based on the following equation: $COM_d = 0.180\times FCI + 2.73\times C_{OL}+1.23\times(C_{UT}+C_{WT}+C_{RM})$. Here, the fixed capital investment (FCI) is estimated as the sum of all equipment costs. In order to calculate a cash flow diagram, we assumed a tax rate of 35% and an annual interest rate of 10%, considering the revenue from this project. The After-Tax Cash Flow is defined as follows:

$$(revenue - COM_d - depreciation)(1 - t) + depreciation$$

Since the lifetime of a chemical plant is assumed to be 10 years, depreciation is considered as 10% of fixed capital investment.

We started the profitability analysis in the most conservative condition with 99% product price discounted and pyrrole as the only liquid product. The profitability analysis (CH_4/N_2 = 1) shows the revenue from selling products is only $0.89 million, while the COM_d reaches $2.61 million. Therefore the after-tax cash flow can be determined as (-)$1.09 million per year suggesting that the project is not feasible due to the extremely low revenue relative to the cost of manufacturing. In case the price of our products increases to 5% of commercial price (i.e., 95% discount), the revenue climbs to $4.43 million as a result of highly-valued pyrrole and propyne. The after-tax cash flow reaches $1.21 million per year with a payback period of 0.8 year (Table 7), indicating that the plant has become highly profitable. With the CH_4/N_2 = 1/3 process considering a product price at 5% of the commercial price, both revenue and COM_d per year increase by $0.1 million compared with the result of CH_4/N_2 = 1 due to higher yield of pyrrole, even though we have a higher cost for the plasma reactors/raw materials. As a result, the profitability of the project is not strongly influenced by the CH_4/N_2 ratio.

However, in the case of enhancing the yield/selectivity to other N-containing products than pyrrole, the process is estimated to see significant profits. Our results show the liquid products from the plasma reactor not only contain pyrrole, but also includes higher-value products such as

methyl triazole and proline, which are worth $11020/kg and $20800/kg, respectively (99% bulk discounted prices). Based on the mole fraction from experimental results, the average price of 14 N-containing liquid products was calculated at $236/mol (Table A1), while pure pyrrole is only worth $0.717/mol. Assuming the total flow rate of N-containing products is consistent with pyrrole (45.5 mol/h) and all the products are sold, the revenue of this plant would increase to over $90 million rather than $0.89 million with the discounted cash flow rate of return of 978% (Table 7). As the CH_4/N_2 ratio was changed to 1/3, the yield of liquid products increased from 45.5 mol/h to 67 mol/h as well as a revenue increase from $90 million to $132 million. Therefore, the profitability of the project was further improved by controlling the CH_4/N_2 ratio (Table 7). These results suggest that producing N-containing products from shale gas and N_2 is necessary. However, the separation of these N-containing products is not trivial and will consume additional energy and increase the capital investment. However, the product stream could be sold as a mixture at a reasonable discounted price for a chemical company to perform the separations. Another solution is to improve the selectivity to most valuable N-containing products, such as methyl triazole and proline.

However, tuning the selectivity of products by the plasma alone will be challenging. In order to improve the selectivity to certain products will involve coupling the plasma with appropriate catalysts. As one of the examples, we have demonstrated in our previous work that activation of hydrogen and nitrogen is highly promoted by the interaction between metal catalysts and the plasma environment to produce ammonia. Further, the yield of ammonia over metal surfaces can exceed the equilibrium limit, which highlights the synergies between the plasma and catalyst. Similar enhancing effects could also be discovered in CH_4/N_2 coupling reactions by screening and searching for appropriate catalysts. Therefore, our next step of the experimental portion of the project will focus on the evaluation of various catalysts to control the selectivity to various N-containing products.

Table 7. Profitability analysis and sensitivity to feed composition and product price.

Condition	Revenue (Million $)	COM_d (Million $)	After-tax cash flow per year (Million $)	Net Present Value (Millions$)	Discounted Cash Flow Rate of Return	Discounted Payback Period (years)
$CH_4/N_2 = 1$ with 99% price discount	0.89	2.61	-1.09	-6.4	-	-
$CH_4/N_2 = 1$ with 95% price discount	4.43	2.61	1.21	5.31	82.5%	0.8
$CH_4/N_2 = 1/3$ with 95% price discount	4.56	2.72	1.23	5.29	74.3%	0.9
$CH_4/N_2 = 1$ with 99% price discount w/ avg. price of all liquid products	90	2.61	56.83	287	978%	0.017
$CH_4/N_2 = 1/3$ with 99% price discount w/ avg. price of all liquid products	132	2.72	84.51	428	>1000%	0.013

6. CONCLUSIONS

The final TEA has provided important information about the potential scale-up of the ND plasma CH_4-N_2 coupling technology. It is apparent that the plasma reactor will be a significant capital cost and may need additional engineering/design for proper operation under these conditions. The electricity costs to power the plasma reactor are also a significant portion (~78%) of the total utility costs. Furthermore, the use of renewable energy to power the plasma reactor would further increase the electricity costs and may be necessary to include if the well-head is off the grid in remote locations.

Although the capital and operating costs are relatively high, the profitability analysis suggests that the process is more sensitive to the product composition and product value. This result allows us to focus our efforts on increasing the selectivity of the reaction network to more valuable products by further varying the inputs to the reactor (e.g., gas composition, flow rate, temperature, specific energy input, etc.) or by incorporating the appropriate catalyst. Overall, it is apparent that this process has a high potential for commercialization.

7. REFERENCES

1. Emam, E. A., Petroleum & Coal 2015, 57 (5), 532-555.
2. US Energy Information Administration: https://www.eia.gov/naturalgas/.
3. Diefenbach, M.; Brönstrup, M.; Aschi, M.; Schröder, D.; Schwarz, H., HCN Synthesis from Methane and Ammonia: Mechanisms of Pt+-Mediated C−N Coupling. J. Am. Chem. Soc. 1999, 121 (45), 10614-10625.
4. Grabow, L. C.; Studt, F.; Abild-Pedersen, F.; Petzold, V.; Kleis, J.; Bligaard, T.; Norskov, J. K., Descriptor-Based Analysis Applied to HCN Synthesis from NH3 and CH4. Angew. Chem. International Ed. 2011, 50 (20), 4601-4605.
5. Gail, E.; Gos, S.; Kulzer, R.; Lorosch, J.; Rubo, A.; Sauer, M., Cyano Compounds, Inorganic. Ullmann's Encyclopedia of Industrial Chemistry 2000, https://doi.org/10.1002/14356007.a08_159.
6. National Energy Technology Laboratory. Techno-economic analysis guides energy research toward success. https://www.netl.doe.gov/node/3389.
7. Hotchkiss, T.; Sczentes, K.; Joyce, T., ND IDEA Center Internal Discussion/Communication. Jan. 2020.
8. https://www.marketsandmarkets.com/PressReleases/fungicides.asp.
9. Bullin, K.; Krouskop, P., Composition Variety Complicates Processing Plans for US Shale Gas. Proceedings of the Annual Forum, Gas Processors Association: Houston, TX, USA, 2008.
10. Ashour, I.; Al-Rawahi, N.; Fatemi, A.; Vakili-Nezhaad, G., Applications of Equations of State in the Oil and Gas Industry. Thermodynamics-Kinetics of Dynamic Systems 2011, 165–178.
11. Singh, L. K., Optimize compressor parameters for reduced inlet pressure and gas flow. http://gasprocessingnews.com/features/201410/optimize-compressor-parameters-for-reduced-inlet-pressure-and-gas-flow.aspx.
12. Turton, R., Analysis, Synthesis, and Design of Chemical Processes, Third Edition, Prentice Hall. 2012.
13. Kogelschatz, U., Dielectric-barrier Discharges: Their History, Discharge Physics, and Industrial Applications. Plasma Chemistry and Plasma Processing 2003, 23.
14. Delikonstantis, E.; Scapinello, M.; Stefanidis, G. D., Investigating the Plasma-Assisted and Thermal Catalytic Dry Methane Reforming for Syngas Production: Process Design, Simulation and Evaluation. Energies 2017, 10, 1429.

8. SUPPORTING TABLES/FIGURES

Table A1. Prices of identified liquid hydrocarbons and N-containing compounds from experimental results. The average bulk discount price is determined as:

$$price_{avg} = \frac{\sum(mole\ fraction \times price)}{\sum(mole\ fraction)} = \$236/mol$$

Product Name	Amount	Price	Cost per g (or mL)	Cost per lb	Bulk Discount of 99% (price/kg)	Approximated mole fraction in liquid based on GC peak area (%)
Pyrrole	25 mL	$27.90	$1.12	$506	*$11*	*6.252*
Triazole	25 g	$30.80	$1.23	$559	*$12*	*4.133*
Methyl Pyrazole	10 g	$118.00	$12	$5,352	*$118*	*4.167*
Methyl Triazole	50 mg	$55.10	$1,102	$499,859	***$11,020***	***3.307***
Proline	10 mg	$20.80	$2,080	$943,473	*$20,800*	*3.086*
Pyramidine amine	100 g	$39.60	$0.40	$180	*$4*	*5.701*
Triazine	1 g	$37.60	$38	$17,055	*$376*	*5.758*
Amino Pyrazine	10 g	$93.30	$9	$4,232	*$93*	*3.056*
Dimethyl Pyrazole	5 g	$31.20	$6	$2,830	*$62*	*2.467*
Piperidinamine	100 mg	$55.10	$551	$249,930	*$5,510*	*2.302*
Dimethyl Imidazole	5 g	$17.30	$3	$1,569	*$35*	*2.063*
Immidazole	5 g	$57.70	$12	$5,234	*$115*	*2.602*
Methyl Formamide Acetamide	100 mL	$28.70	$0.29	$130	*$3*	*4.934*
(Butylamino) Acetonitrile	25 g	$264.00	$11	$4,790	*$106*	*4.602*
Ethylene Amine	5 mL	$31.10	$6	$2,821	*$62*	*1.616*
Hexane	1 L	$132.00	$0.13	$60	*$1*	*1.547*
Methyl Pentadiene	5 mL	$101.00	$20	$9,163	*$202*	*1.839*

Figure A1. ND IDEA Center Risk Scorecard for the production of N-containing liquids via plasma stimulation.

Table A2. Stream table for feed streams through the reactor in the simulated ND process for CH_4:N_2 (1:3).

	F-1A	F-2A	F-1B	F-2B	F-3	F-4	P-1	P-2
Temperature (°C)	25	25	10.5	22.95	19.3	200	200	35
Pressure (bar)	30.4	10.0	2.0	2.0	2.0	2.0	1.2	1.2
Flows (kg/hr)								
Methane	39.95	0.0	39.95	0.0	39.95	39.95	33.1	33.1
Nitrogen	0.0	209	0.0	209	209	209	207	207
Ethane	0.0	0.0	0.0	0.0	0.0	0.0	0.40	0.40
Ethylene	0.0	0.0	0.0	0.0	0.0	0.0	0.07	0.07
Ammonia	0.0	0.0	0.0	0.0	0.0	0.0	1.15	1.15
Hydrogen	0.0	0.0	0.0	0.0	0.0	0.0	0.91	0.91
Propane	0.0	0.0	0.0	0.0	0.0	0.0	0.03	0.03
Propylene	0.0	0.0	0.0	0.0	0.0	0.0	0.01	0.01
Methyl Acetylene	0.0	0.0	0.0	0.0	0.0	0.0	1.62	1.62
Pyrrole	0.0	0.0	0.0	0.0	0.0	0.0	4.51	4.51

Table A3. Stream table for streams entering the staged compression sequence through the end of the system in the simulated ND process.

	P-3	P-4	P-5	P-6	P-7	P-8	P-VAP	P-LIQ
Temperature (°C)	175	40	165	58	117	-20	20	20
Pressure (bar)	3.6	3.6	9.5	9.5	15	15	1	1
Flows (kg/hr)								
Methane	33.1	33.1	33.1	33.1	33.1	33.1	33.1	3.3×10^{-4}
Nitrogen	207	207	207	207	207	207	207	3.1×10^{-4}
Ethane	0.40	0.40	0.40	0.40	0.40	0.40	0.40	5.1×10^{-5}
Ethylene	0.07	0.07	0.07	0.07	0.07	0.07	0.07	5.4×10^{-6}
Ammonia	1.15	1.15	1.15	1.15	1.15	1.15	1.14	0.0037
Hydrogen	0.91	0.91	0.91	0.91	0.91	0.91	0.91	3.0×10^{-7}
Propane	0.03	0.03	0.03	0.03	0.03	0.03	0.03	1.4×10^{-5}
Propylene	0.01	0.01	0.01	0.01	0.01	0.01	0.01	7.3×10^{-6}
Methyl Acetylene	1.62	1.62	1.62	1.62	1.62	1.62	1.62	0.0047
Pyrrole	4.51	4.51	4.51	4.51	4.51	4.51	0.42	4.09

Table A4. Total equipment cost for CH_4:N_2 = 1/3 process

Equipment Name	Equipment ID	Purchase Cost ($)
Compressor	C-101	34,900
Compressor	C-102	34,900
Compressor	C-103	34,900
Heat Exchanger – 1	E-101	65,800
Heat Exchanger – 2	E-102	57,100
Heat Exchanger – 3	E-103	57,100
Heat Exchanger – 4	E-104	57,600
Heat Exchanger – 5	E-105	58,100
Flash Drum	V-101	12,800
Plasma Reactor (2 reactors, 348 tubes per reactor)	Z-101	535,879
Total Equipment Cost		**$946,378**

Table A5. Total annual utility cost for CH_4:N_2 = 1/3 process

Utility	Annual Utility Cost ($)
Low Temperature refrigerated water (5)	5,273
Electricity	79,486
Natural gas for heating reactor	6,362
High pressure steam	0
Low Temperature refrigerant (-50)	5,554
Total Annual Utility Cost	**$98,600**